Empirically Interrelating Stellar Chromospheric Activity, Photometric Variability and Radial Velocity Variations to Enhance Planet Discovery

By

Fabienne Anne Bastien

Dissertation

Submitted to the Faculty of the

Graduate School of Vanderbilt University

in partial fulfillment of the requirements

for the degree of

DOCTOR OF PHILOSOPHY

in

Physics

May 2014
Nashville, Tennessee

Approved:

Dr. Keivan G. Stassun

Dr. David A. Weintraub

Dr. C. Robert O'Dell

Dr. Kenneth G. Carpenter

Dr. James H. Dickerson

ACKNOWLEDGMENTS

Because I am bound to forget to mention some of those who crossed my path over the course of this thesis effort and yet to whom I owe a debt of gratitude for their help and presence over the course of this challenging but rewarding time, I wish to keep this simple:

To all those who supported and encouraged me
in my attempts to pursue my dreams,
and to all those who encouraged me to become
more than I thought I could be,

Thank you from the bottom of my heart.

This effort was funded in part by a GAANN fellowship, a NASA Harriet Jenkins predoctoral fellowship and a Vanderbilt Provost graduate fellowship.

Table of Contents

List of Tables

Table Page

List of Figures

CHAPTER 1

INTRODUCTION

1.1 STATEMENT OF THE PROBLEM

Processes occurring on the surfaces of stars induce photometric and radial velocity (RV) variations that have traditionally been largely attributed to dark magnetic spots, analogs to Sun spots. These variations, while informing us about surface features on stars other than the Sun, are a significant impediment to the detection of extrasolar planets, particularly Earth-like ones: RV noise, or "jitter," can wash out or even mimic the signatures of extrasolar planets [103], and photometric "noise" can similarly preclude the detection of the tiny transit signature of an Earth-like planet. Because of this, exoplanet detection surveys preferentially target "quiet" stars, those that, in the photometric domain, exhibit low levels of photometric variability or, in the RV domain, low levels of chromospheric activity which is known, as informed by the Sun, to correlate with low spot activity and by experience to more or less correlate with low RV noise. Even when targeting "quiet" stars, however, there are stellar variations that can still bar the detection of Earth-like exoplanets. Among these are granulation and low-level pulsations, and their contributions to the observed stellar noise have largely been examined in the RV domain and are based on the only example of a main-sequence star for which these variations have until recently been observed: the Sun [46, 47, 99].

1.2 EARLY INVESTIGATIONS AND CURRENT STATE OF THE FIELD

The study of the manifestations of chromospheric activity in the RV and photometric domains has a long history, particularly in the realm of stellar astrophysics; only fairly recently have these manifestations been considered in the realm of extrasolar planet detection. Early works found that chromospherically active stars tend to be rapid rotators, and rapid rotation is an indicator of youth on the main-sequence [123]. This connection is now frequently used to estimate the ages of field stars with $\sim$30% uncertainty [15, 16]. It is also used to exclude chromospherically active stars from extrasolar planet surveys, as rapid rotation can induce RV variations greater than 100 m s^{-1} [116, 143], even when the photometric amplitude, another indicator of chromospheric activity, is very low (i.e., less than 3 parts per thousand (ppt)) [21].

That even low amplitude variable, and therefore presumably chromospherically inactive, stars can exhibit such high levels of RV jitter is rather unexpected given the long established correlation between photometric amplitude and chromospheric activity determined by the Mount Wilson survey [48, 12, 86, 111]. This survey has monitored the chromospheric activity of nearly 2000 stars since 1966 and has defined our current view of magnetic activity variations on other stars, including the fact that not all Sun-like stars show Sun-like magnetic activity cycles [12]. Results from this survey determined that photometric amplitude may be used as a proxy for the level of chromospheric activity, and this is now frequently used in instances where no spectroscopic measurement of chromospheric activity is available [35, 18, 138]. These Mount Wilson photometric results, however, were found using ground-based telescopes, and as such were not even sensitive to Sun-like photometric amplitudes; the Sun's photometric amplitude only reaches ∼2 ppt at solar maximum. It would take space-based photometric surveys, particularly those designed to search for Earth-like extrasolar planets and hence with up to parts per million photometric precision together with a rapid cadence and long, uninterrupted observation windows, to enable research into truly Sun-like photometric variations.

1.3 OPEN QUESTIONS

Space-based photometric missions, like *MOST* [137], CoRoT [11] and *Kepler* [25], have unveiled an unexpectedly wide variety of photometric behaviors in Sun-like stars, much of it occurring at very low photometric amplitudes. They have also, for the first time, enabled us to place the Sun in a representative context [17, 19]. The newly revealed photometric behaviors are poorly understood and, as a result, so is their connection with chromospheric activity and RV jitter.

This has important implications for both our understanding of the Sun's place among stars and our ability to detect small extrasolar planets. Indeed, early results from the *Kepler* mission, whose goal was to find Earth-like planets, found that Sun-like dwarf stars are photometrically noisier than expected, implying that the Sun is an unusually quiet star [56]. The high noise levels, above and beyond that expected from chromospheric activity, indicated a need to revise the expected performance of the mission in finding Earth-like planets. Others, however, argue that the Sun behaves as expected and that the high noise levels are instrumental in origin [17, 18, 19]. The debate ultimately has implications for how completely and effectively we can place constraints on the prevalence of Earth-like planets around Sun-like stars. It also impacts the prioritization of planet candidate RV follow-up: for instance, the stars in the *Kepler* field are faint for RV surveys, and hence large telescopes are heavily relied upon. As such, it is imperative, if the primary goal is to find Earth-like planets, to ensure that the stellar noise properties are well-understood, both those in the photometric domain and those expected in the RV domain, in order to properly disentangle planetary signals from those of stellar origin. An additional and underappreciated wrench in the problem is the fact that these ensemble studies of Sun-like stars are based on poorly known fundamental stellar parameters, in particular the stellar evolutionary state.

A number of studies have attempted to leverage the unprecedented quality of the data coming out of these space-based photometric missions to gain a greater handle on stellar noise. On the photometric front, most of them have focused on stellar rotation [138, 112, 95, 96], with the primary goal of placing observational constraints on dynamo theories. The RV domain has received significantly less attention, with efforts being focused on using spot models to predict the expected level of RV jitter given a high quality light curve [4, 24]. However, the newly available high quality photometric data provide an opportunity to examine contributions to stellar noise other than magnetic spots and to extend our definition of ”photometric variability” beyond amplitude and rotation. We may now empirically approach the problem of stellar noise from a new angle, focusing in the photometric domain on new ways of characterizing stellar variability and with the end aim of opening new planet discovery domains.

1.4 SUMMARY OF THE THESIS

In this thesis, we sought to empirically interrelate stellar chromospheric activity, photometric variability and RV jitter, extending previous studies into the realm of the recently revealed and poorly understood photometric variations. Our end goal was to use the derived relations to robustly characterize stellar noise in the photometric and RV domains in order to enhance exoplanet detection and characterization.

In Chapter 2, we deviate from this core goal to demonstrate how even ground-based, rapid cadence observations can reveal unexpected stellar variations that may be traced to dynamic processes that influence and inform us about their evolution. We use high cadence photometric observations to study short timescale variations during the outburst of an eruptive pre-main sequence star, V1647 Orionis. These rare and poorly understood outbursts are thought to be driven by a perturbation to the circumstellar accretion disk driving disk material onto the star, resulting in a rapid increase in both the accretion rate and brightness of the object by several orders of magnitude. Using the first set of observations to probe this time domain in one of these events, we discovered a transient periodic signal during the rise phase of one of these outbursts which we show may correspond to short-lived radial pulsations of the star driven by the surge in the accretion rate.

In Chapter 3, we make use of the space-based photometric mission *Kepler* to examine the photometric noise of older field stars. We suggest that the photometric noise we examine, “flicker,” traces granulation, and we show that it provides a new and simple way to measure stellar surface gravity. We find that “flicker” enables the measurement of this quantity with a precision of 0.1 dex, and we use it, together with two other simple measures of photometric variability, to construct an evolutionary diagram that traces the photometric evolution of Sun-like stars from the main sequence out towards the red giant branch.

Chapter 4 leverages the knowledge gleaned from Chapter 3 to provide insight into RV jitter. We compare RV jitter measurements of a sample of stars in the *Kepler* field with different ways of characterizing the stellar photometric variations in their *Kepler* light curves. We not only find that RV jitter manifests in the Fourier spectrum of a high quality light curve, but we also demonstrate that we can quantatively predict a star's expected level of RV jitter from the evolutionary diagram presented in Chapter 3. In particular, we demonstrate that spot models used to predict RV jitter systematically underpredict it for low amplitude variable stars, and we suggest that granulation is a more important contributor to RV jitter than has previously been appreciated.

To close the thesis, Chapter 5 suggests that, using "flicker"-based surface gravities, the bright transiting planet candidate host stars in the *Kepler* field may be ∼30% larger than expected from broad-band photometric and spectroscopic measurements of surface gravity. The result is that the median planet candidate radius, determined from that of the host star, is also larger than expected. We find that the discrepancy may be tied to an underappreciated astrophysical bias present in magnitude-limited surveys but hidden when strong priors favoring the main sequence are used in determining fundamental stellar parameters.

Chapter 2

HIGH CADENCE TIME-SERIES PHOTOMETRY OF V1647 ORIONIS

We present high cadence (1–10 hr^{-1}) time-series photometry of the eruptive young variable star V1647 Orionis during its 2003–2004 and 2008–2009 outbursts. The 2003 light curve was obtained mid-outburst at the phase of steepest luminosity increase of the system, during which time the accretion rate of the system was presumably continuing to increase toward its maximum rate. The 2009 light curve was obtained after the system luminosity had plateaued, presumably when the rate of accretion had also plateaued. We detect a 'flicker noise' signature in the power spectrum of the lightcurves, which may suggest that the stellar magnetosphere continued to interact with the accretion disk during each outburst event. Only the 2003 power spectrum, however, evinces a significant signal with a period of 0.13 d. While the 0.13 d period cannot be attributed to the stellar rotation period, we show that it may plausibly be due to short-lived radial oscillations of the star, possibly caused by the surge in the accretion rate.

2.1 INTRODUCTION

On 9 February 2004, McNeil [93] discovered a previously unknown object about 12 arcminutes south-west of the M78 reflection nebula. Studies of images of the area taken prior to the event confirmed that a star, V1647 Orionis, had brightened

---

[0] A version of this chapter was published in *The Astronomical Journal*, vol. 142, pp141-148 (2011).

significantly over the course of a few days, illuminating the material surrounding it and creating what is now known as McNeil's Nebula. Briceño et al. [28], through their long-term survey of the Orion Nebula region, constrained the onset of the outburst to early November 2003. The lightcurve obtained by Acosta-Pulido et al. [2] shows that the object reached maximum brightness by the beginning of March 2004 and had faded back to its initial state by March 2006. In examining photographic plates from the Asiago and Harvard Observatories, Aspin et al. [8] found that this star had undergone a similar eruption in 1966, fading back to invisibility by the end of November 1967. In 2009, Aspin et al. [10] reported that yet another outburst event began in August 2008.

The rare nature of these events in general, and the fact that we have been able to observe several of them from one star in particular, give us a unique opportunity to study such stellar outbursts within the context of star formation. Here, we present high cadence time-series photometry of V1647 Orionis from its 2003–2004 and 2008–2009 eruptions.

2.2 LIGHT CURVE OBSERVATIONS AND REDUCTIONS

We observed V1647 Ori during a nine-night observing run in 2003 December with the Mosaic-1 wide-field imager on the WIYN 0.9-m telescope at the Kitt Peak National Observatory. This instrument consists of eight 2048×4096 pixel CCDs with a plate scale of $0\farcs43$ pix^{-1} and total field of view of $59' \times 59'$. Four of the nine nights were lost to poor weather. We used the SDSS z filter at 9400Å to obtain a total of 65 images on five nights with an average cadence of $\sim$1 hr^{-1}. The exposure time for all images, except those taken on the first night, was 120 s. On the first night, we took shorter exposures that were 60 s as well as longer ones of 180 s. The observations were obtained at airmasses ranging from 1.8 to 2.5. This dataset samples the time during which the source's brightness was steeply increasing (cf. Fig. 2.1).

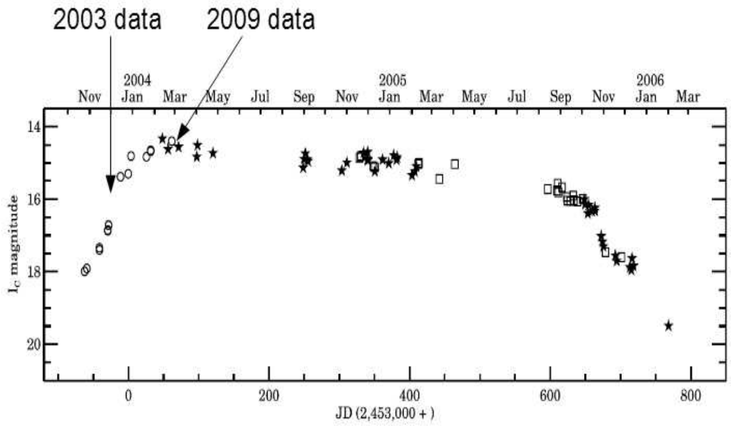

Figure 2.1: Our datasets in context. The 2003 data were taken in 2003 December, during the phase of steepest increase in brightness. No outburst lightcurve has yet been published for the 2008-2009 event, but if we assume a rise-time similar to the 2003-2004 outburst, our 2009 data would sample the phase when the brightness of V1647 Ori had plateaued, as shown. Different symbols denote observations from different observing campaigns [2]. Adapted from Acosta-Pulido et al. [2].

We used the Y4KCam on the SMARTS 1.0-m telescope at the Cerro Tololo Inter-American Observatory to observe V1647 Ori on UT 2009 January 23. The 4064×4064 CCD has a plate scale of $0\farcs289$ pix^{-1} and a field of view of $20'\times20'$. We used the I_C filter for our 32 images taken with an average cadence of $\sim$10 hr^{-1}. The exposure time for each image was 300 s and the range in airmass was 1.2 to 2.6. If we assume a rise time similar to the 2003 outburst, then these data were taken soon after the object peaked in brightness (Fig. 2.1).

In order to measure how the star's brightness changed with time, we performed aperture photometry using standard IRAF routines[1]. We used an aperture radius of 6 pixels and measured the sky background with a 5-pixel wide annulus and a 10-pixel inner radius for the 2003 data; we used an 8-pixel inner radius for the 2009 data. We selected these parameters based on the average seeing of the two datasets (3.6 pixels in 2003 and 3.0 pixels in 2009).

We performed differential photometry because the observing conditions were non-photometric in both 2003 and 2009. Because most of the stars in this field are likely variable, we did not attempt to choose a single comparison star with which to determine the differential light curve of V1647 Ori. We expect that on average any variations in the field stars are uncorrelated except for effects of the instrument and sky conditions. Thus we selected five calibration stars (Table 2.1) in the vicinity of the McNeil's object that were of comparable brightness to V1647 Ori with which we defined an average "reference star." We checked that none of these are known to be variables. We further checked that the differential light curve of each of these stars, determined relative to the other four calibration stars, was not variable within the photometric errors.

The full differential light curve from 2003 December is presented in Table 2.2 and from 2009 January in Table 2.3. The errors on individual photometric measurements are typically 0.02 mag in the 2003 data and 0.01 mag in the 2009 data, which include

---

[1] IRAF is distributed by the National Optical Astronomy Observatories, which are operated by the Association of Universities for Research in Astronomy, Inc., under cooperative agreement with the National Science Foundation.

Table 2.1. J2000 coordinates of stars used for differential photometry

RA[a]	Dec[b]
05:46:22	-00:03:37
05:46:29	-00:03:47
05:46:31	-00:04:21
05:46:28	-00:09:59
05:46:26	-00:10:25

[a] in hh:mm:ss

[b] in dd:mm:ss

both the formal photometric errors of V1647 Ori and the error of the mean of the combination of the five comparison stars.

Table 2.2: Differential photometric measurements of V1647 Ori in 2003 December

Julian Date(+2450000)	Δz	$\sigma_{\rm mag}$
2978.7040	0.000	0.046
2978.7100	0.020	0.032
2978.7410	-0.034	0.051
2978.7440	-0.026	0.032
2978.7560	-0.020	0.048
2978.7590	-0.073	0.028
2978.7710	-0.005	0.047

Table 2.2 – Continued

Julian Date(+2450000)	Δz	$\sigma_{\rm mag}$
2978.7740	0.014	0.029
2978.8000	0.095	0.046
2978.8040	0.056	0.029
2978.8300	0.194	0.049
2978.8330	0.082	0.028
2978.8580	-0.012	0.041
2978.8620	0.045	0.028
2978.8890	-0.021	0.044
2978.8930	-0.026	0.025
2978.9200	0.150	0.050
2978.9230	0.101	0.028
2978.9510	0.182	0.053
2978.9540	0.021	0.027
2978.9790	0.021	0.053
2978.9810	-0.019	0.030
2979.0060	-0.089	0.053
2979.0090	-0.028	0.034
2982.7000	-0.661	0.030
2982.7320	-0.725	0.024

Table 2.2 – Continued

Julian Date(+2450000)	Δz	σ_{mag}
2982.7610	-0.648	0.028
2982.7900	-0.782	0.022
2982.8190	-0.863	0.022
2982.8600	-0.769	0.020
2982.8890	-0.673	0.023
2982.9850	-0.687	0.026
2983.6870	-0.690	0.022
2983.7150	-0.729	0.021
2983.7440	-0.723	0.019
2983.7720	-0.719	0.019
2983.8000	-0.705	0.018
2983.8290	-0.713	0.018
2983.9340	-0.656	0.021
2983.9650	-0.790	0.020
2983.9940	-0.833	0.021
2984.6570	-0.998	0.017
2984.6710	-0.963	0.018
2984.7200	-0.939	0.016
2984.7490	-1.011	0.015

Table 2.2 – Continued

Julian Date(+2450000)	Δz	σ_{mag}
2984.7780	-1.063	0.015
2984.8060	-1.045	0.014
2984.8350	-0.981	0.015
2984.8730	-1.081	0.014
2984.9020	-1.149	0.015
2984.9300	-1.056	0.016
2984.9600	-1.068	0.016
2984.9910	-1.033	0.017
2986.6640	-1.569	0.011
2986.6920	-1.636	0.009
2986.7210	-1.668	0.010
2986.7490	-1.695	0.009
2986.7780	-1.619	0.009
2986.8060	-1.589	0.010
2986.8340	-1.674	0.008
2986.8620	-1.661	0.009
2986.8910	-1.592	0.011
2986.9240	-1.570	0.012
2986.9520	-1.599	0.012

Table 2.2 – Continued

Julian Date(+2450000)	Δz	$\sigma_{\rm mag}$
2986.9800	-1.635	0.013

Table 2.3: Differential photometric measurements of V1647 Ori in 2009 January

Julian Date(+2450000)	ΔI	$\sigma_{\rm mag}$
4854.6518	0.023	0.008
4854.6576	0.000	0.006
4854.6628	0.017	0.006
4854.6665	-0.019	0.007
4854.6702	0.015	0.008
4854.6739	-0.010	0.008
4854.6776	-0.000	0.007
4854.6854	0.000	0.009
4854.6891	0.037	0.009
4854.6927	-0.009	0.008
4854.6964	-0.003	0.008
4854.7003	-0.030	0.010

Table 2.3 – Continued

Julian Date(+2450000)	ΔI	$\sigma_{\rm mag}$
4854.7042	0.019	0.007
4854.7079	-0.006	0.009
4854.7116	0.061	0.009
4854.7153	0.019	0.009
4854.7190	0.045	0.010
4854.7229	-0.011	0.009
4854.7266	-0.047	0.008
4854.7302	-0.022	0.010
4854.7339	0.046	0.008
4854.7376	-0.063	0.009
4854.7414	0.022	0.012
4854.7451	-0.031	0.008
4854.7487	0.013	0.012
4854.7524	0.043	0.011
4854.7561	-0.030	0.011
4854.7601	0.002	0.010
4854.7637	0.008	0.011
4854.7674	0.002	0.012
4854.7711	-0.007	0.011

Table 2.3 – Continued

Julian Date(+2450000)	ΔI	σ_{mag}
4854.7748	-0.040	0.012

2.3 RESULTS

2.3.1 2003 light curve

2.3.1.1 Variability

Our data show that V1647 Ori brightened by almost 2 mag over the course of our 9-night run in 2003 December (Fig. 2.2, *top*). This steep rise in brightness is approximately linear (in magnitudes), but with low-level structure superposed on top of the linear trend. To explore the structure of these low-level brightness variations, we de-trended the light curve as follows.

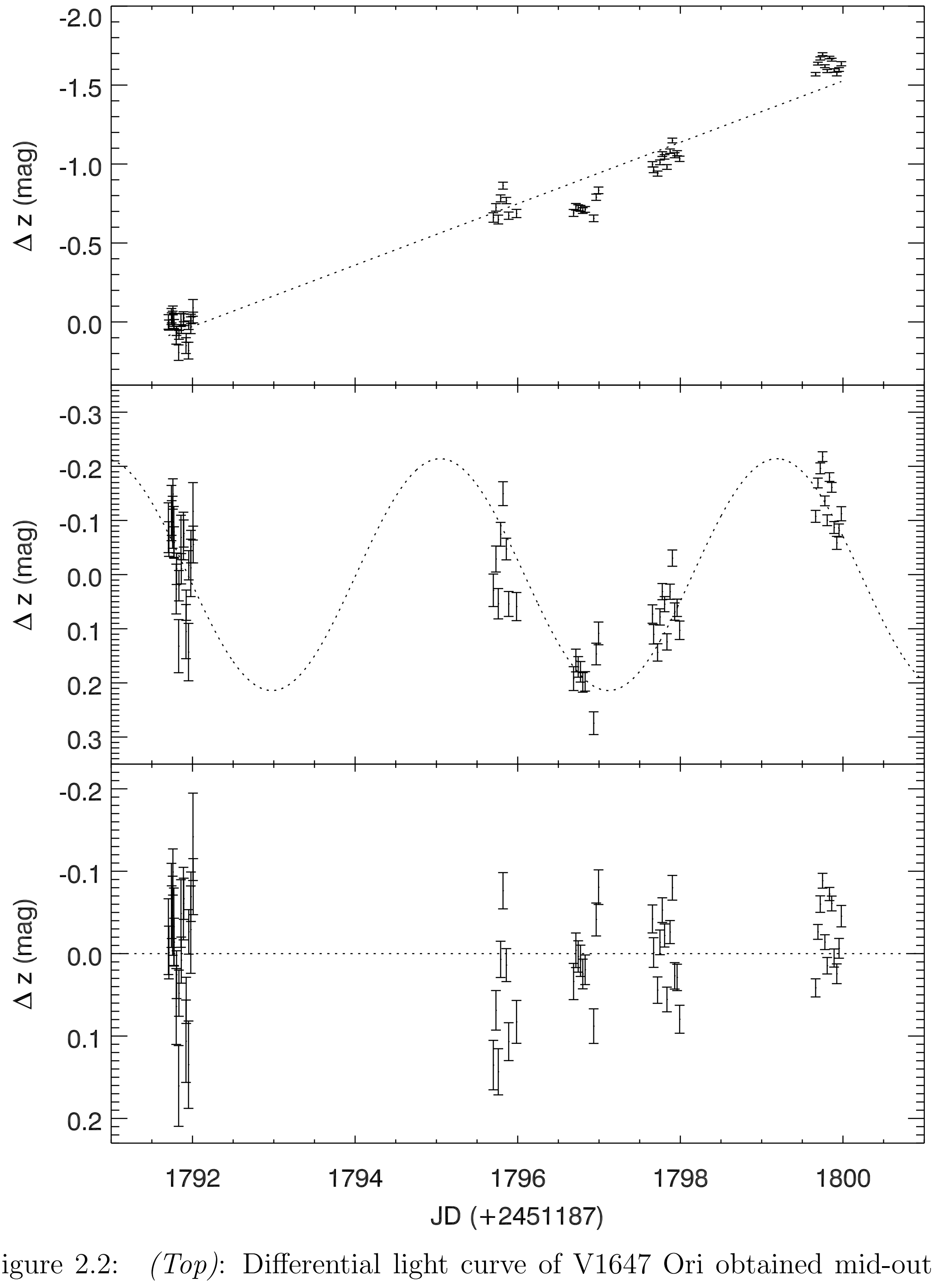

Figure 2.2: *(Top)*: Differential light curve of V1647 Ori obtained mid-outburst in 2003 December. The system brightened by ∼ 2 mag over the course of 9 nights. For reference, the dotted line represents a linear trend fit to the data. The scale of the time axis has been chosen to allow direct comparison with the long-term light curve data presented in Briceño et al. [28, cf. their Fig. 3]. *(Middle)*: Same light curve de-trended with the linear trend from *top*, revealing a quasi-periodic modulation with a timescale of ∼4 d. For reference, the dotted curve represents a sinusoidal trend fit to the data (P=4.14 d). *(Bottom)*: Same light curve further de-trended with the sinusoidal trend from *middle*, revealing short-timescale variations with amplitude ∼0.05 mag.

First we subtracted a linear fit (Fig. 2.2, *top*, dashed line), which reveals a slow brightness variation with a peak-to-peak amplitude of ∼0.3 mag (Fig. 2.2, *middle*). These variations are reminiscent of those commonly observed in classical T Tauri stars, which can arise from variations in the accretion stream or from modulation due to star spots at the stellar rotation period, and which often exhibit periodic or quasi-periodic behavior [Type IIp and Type II, respectively, in the nomenclature of 65] on timescales of ∼1–10 d. The V1647 Ori variations appear to modulate on a timescale of 4–5 d. We cannot establish with our data whether this signal is strictly periodic because our light curve spans only two cycles of such a period, and moreover the data gaps in the light curve leave large phase gaps when the light curve is folded on such a period. Furthermore, we show below that this light curve modulation cannot be the rotation period of the star. In the following we refer to this component of the light curve variability as a "quasi-periodic" modulation. We defer speculation about its possible physical significance to Sec. 4.4.

Next we further de-trended the light curve by subtracting a best-fit sinusoid as a simple representation of the quasi-periodic modulation (P=4.14 d; Fig. 2.2, *middle*, dashed curve). The resulting residual light curve (Fig. 2.2, *bottom*) reveals very short-timescale variations that are significantly larger than the noise in our data (reduced chi-square is $\chi^2_\nu = 9.7$). The amplitude of these variations is $\sigma_{\rm rms} \approx 0.05$ mag.

We conducted a few simple tests to verify that none of the periodic photometric signals discussed here and in what follows correlate with seeing variations. We performed aperture photometry on a portion of the nebula itself using, as before, a 6 pixel aperture radius; we separately performed aperture photometry on V1647 Ori using a larger (9 pixel) aperture radius. We executed a periodogram analysis (as below) on the resultant light curves and also on the seeing variations, which were obtained by measuring the average FWHM of our calibration stars in each image. We found no significant differences in the target light curve, and no evidence for significant periodicities in either the nebular light curve or in the seeing variations (and in particular not at the periods reported below). We conclude that changes in seeing are not driving the periodic photometric variations we report in this work.

2.3.1.2 Periodogram analysis

To examine the light-curve variations of V1647 Ori in detail, we subjected the 2003 light curve (Fig. 2.2) to a standard Lomb-Scargle power spectrum analysis. The Lomb-Scargle periodogram is well-suited to unevenly sampled data such as ours. It moreover possesses well characterized statistical properties that permit quantitative assessment of the statistical significance of any periodic behavior in the data [see 108, and references therein]. We will exploit these statistical properties below.

Fig. 2.3 shows the power spectrum of the non-detrended light curve (Fig. 2.2, *top*) over the frequency range 0.1–18 d^{-1}. The low frequency cutoff corresponds to $1/T$ where T is the total timespan of the data while the high frequency cutoff corresponds to half the sampling frequency (i.e., the Nyquist limit). Overall the power spectrum rises toward smaller frequencies, with a slope that closely approximates a $1/\sqrt{f}$ dependence (represented by dashed/dotted lines in the figure). In addition, the power spectrum exhibits several peaks on top of the $1/\sqrt{f}$ slope. The broad peak at $f \sim 0.2$ d^{-1} corresponds to the slow, quasi-periodic modulation discussed in

Sec. 2.3.1.1 (see also Fig. 2.2, *middle*). The two peaks near $f = 0.8$ d^{-1} and $f = 1.2$ d^{-1} are aliases of the $f \sim 0.2$ d^{-1} modulation beating against the diurnal data gaps ($f = 1$ d^{-1}). The peak near $f = 8$ d^{-1} is due to the short-timescale variability in the detrended light curve (Fig. 2.2 *bottom*).

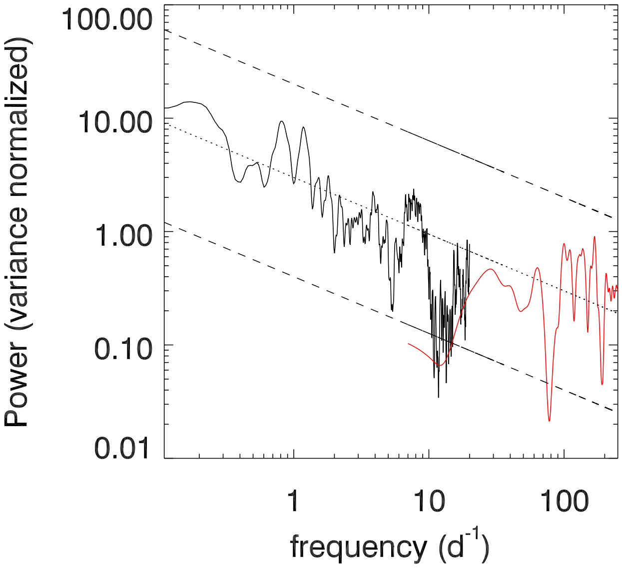

Figure 2.3: Power spectrum resulting from a Lomb-Scargle periodogram analysis of the non-detrended light curve of V1647 Ori, on a log-log scale. The frequency range $0.1 < f < 18$ d^{-1} (black) is provided by the 2003 light curve data (Fig. 2.2, *top*), whereas the frequency range $7 < f < 135$ d^{-1} (red) is provided by the high-cadence 2009 light curve data (Fig. 2.6). Following the usual definition of the Lomb-Scargle periodogram, the ordinate gives the spectral power normalized by the variance of the data. The power spectrum overall follows a slope of $1/\sqrt{f}$ (dashed/dotted lines), and in addition exhibits peaks near frequencies of $\sim$ 0.2, 0.8, 1.2, and 8 d^{-1} (see the text for discussion of the meaning of these peaks).

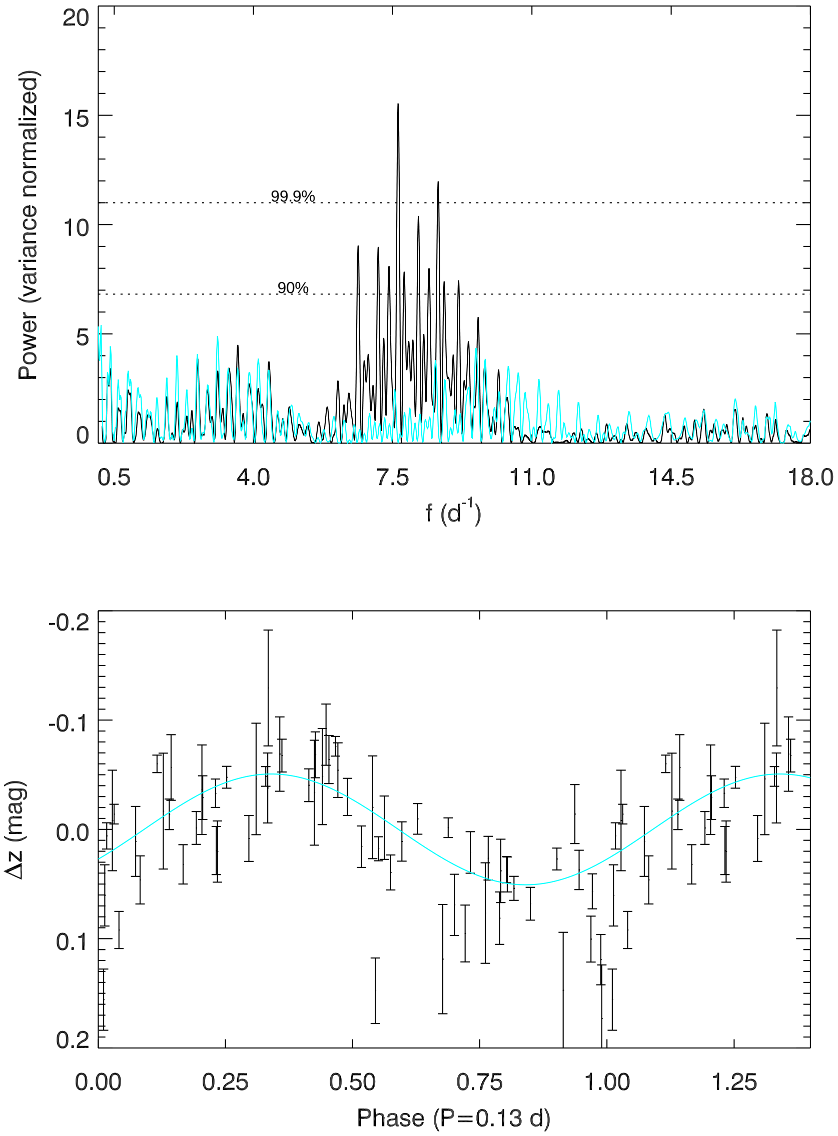

Figure 2.4: *Top:* Power spectrum of the detrended light curve from Fig. 2.2c (black). The highest peak is at 7.7 d^{-1} (a period of 0.13 d). Dotted lines represent the peak heights corresponding to confidence levels of 90% and 99.9%; a peak above the 99.9% confidence line, for example, would have a false-alarm probability (FAP) lower than 0.1%. The signal at 0.13 d, is very highly statistically significant, with a FAP of 1.3×10^{-5}. (See the text and Fig. 2.5 for FAP details.) The blue curve shows the result of removing the 0.13 d period; no significant periods remain. *Bottom:* Light curve data are phased on the 0.13 d period with best-fit sinusoid in blue. The amplitude of the sinusoid is 0.051 mag.

The power spectrum of the detrended light curve is shown in Fig. 2.4 (*top*, black curve). Not surprisingly, nearly all of the power at low frequencies has been eliminated by the de-trending of the linear rise and of the slowly varying quasi-periodic modulation. The power spectrum shows a strong peak at 7.7 d^{-1}, corresponding to a period of 0.13 d, and several other strong features at nearby frequencies, which have power levels corresponding to a statistical confidence of 90% or higher (see below). When we filter out the 0.13-d period peak by subtracting the best fitting sinusoid from the light curve, all of the other statistically significant peaks in the periodogram are also removed (Fig. 2.4, *top*, blue curve), showing them to be aliases and beats of the 0.13 d period. The light curve (Fig. 2.2, *bottom*) is shown folded on this period in Fig. 2.4 (*bottom*), with the best-fitting sinusoid overlaid in blue. The amplitude of this sinusoid is 0.051 mag.

To empirically determine the false-alarm probability (FAP) corresponding to different power levels in the periodogram, we used a Monte Carlo bootstrapping technique as described in Press et al. [108] and implemented in e.g. Stassun et al. [125, 124]. We generated 10,000 artificial light curves by shuffling the actual measurements in temporal order and sampling at the same timestamps as the actual data. In this way, the artificial light curves retain both the noise properties and the time windowing of the real data. For each of the 10,000 artificial light curves, we calculated a power spectrum as for the real data and recorded the power level of the strongest peak in each. The resulting distribution of these 10,000 maximum peak heights gives directly the probability of a given peak height occurring by chance.

The distribution of maximum peak heights is shown in Fig. 2.5 for 10,000 artificial light curves simulating the detrended 2003 light curve (Fig. 2.2, *bottom*). From the figure, peak heights with power levels above ∼7 occur in fewer than 10% of the simulated power spectra, whereas peaks with power levels above ∼11 occur in fewer than 0.1% of the simulated power spectra; these then define the 10% and 0.1% FAP levels, respectively (or equivalently, the 90% and 99.9% confidence levels). These confidence levels are represented by horizontal dotted lines in the observed power spectrum (Fig. 2.4, *top*).

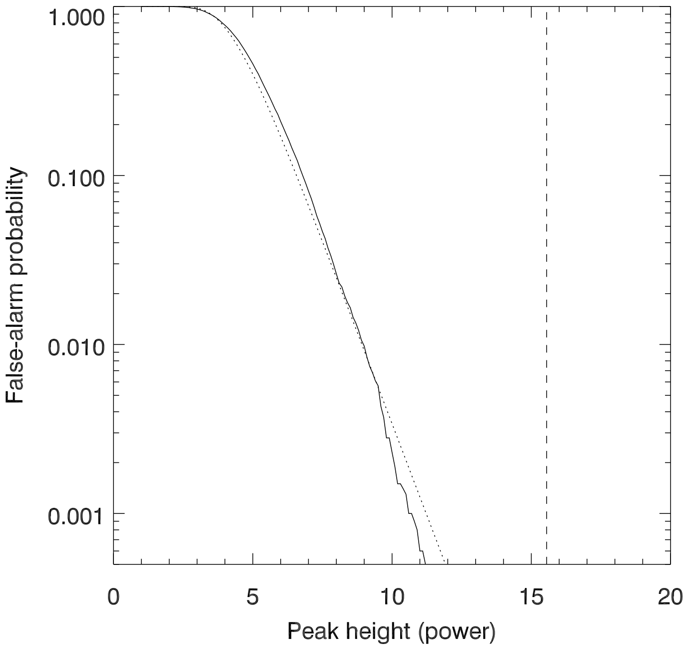

Figure 2.5: The false alarm probability (FAP) of the 0.13 d period as a function of peak height as determined from Monte Carlo simulations. The solid line represents the probability determined from our data, and the dotted curve, which nearly overlays the solid line, shows the analytical probability described by Press et al. [108]. The vertical dashed line shows the peak height we actually observe in Fig. 2.4a. The FAP of the 0.13 d period is 1.3×10^{-5}.

As described by Press et al. [108], the FAP for a given peak height in a Lomb-Scargle periodogram is expected to follow an analytic relationship (cf. their Eq. 13.8.7) shown in Fig. 2.5 as a dotted curve. Evidently, our data and its associated power spectrum closely follow the expected statistical behavior. Fig. 2.5 shows the FAP calculation for the 0.13 d period. The observed peak height (shown as vertical dashed line) has a FAP of 1.3×10^{-5}, and is therefore very highly statistically significant.

We checked that the 0.13 d period and its statistical significance are not dependent on the details of the sinusoidal de-trending that we performed in Sec. 2.3.1.1. As a simple alternative to the sinusoidal detrending (see Fig. 2.2, *middle*), we instead simply shifted all of the data points from a given night such that the mean differential z magnitude for the observations made on each night was 0.0. We then performed the same periodogram analysis as above. We recovered the same 0.13 d period as before with a FAP of 3.6×10^{-5}, again highly statistically significant.

2.3.1.3 Stellar Rotation

Since periodic signals in young, low-mass stars are often associated with rotation, we explored the possibility that we have detected stellar rotation in our light curve. The rotation periods of low-mass pre–main-sequence stars are most typically in the range ∼2–10 d [e.g., 63], though some young low-mass stars have been observed to rotate with periods as short as ~ 0.1 d [125].

Adopting values for the visual extinction (19 ± 2 mag), K-band veiling (1.5 ± 0.2 mag), spectral type ($M0 \pm 2$ subclasses), and K-band apparent magnitude (9.9 mag in February 2007) as determined by Aspin et al. [9], a bolometric correction of

$BC_V = -1.3$ and a $(V - K)$ color of 3.7 as appropriate for an M0 spectral type [78], the equations for absolute K magnitude and bolometric luminosity from Greene & Lada [59], and a distance of 426 ± 20 pc [98, 84, 66], we calculate a stellar radius of $4.2^{+1.0}_{-1.3}$ $R_{\odot}$.

Aspin et al. [10] observed line broadening in the spectrum of V1647 Ori of 120 km s^{-1}. While the spectra of EXor and FUor eruptive variables can be dominated by the hot "atmosphere" of the inner accretion disk during outburst, the Aspin et al. [10] observations were obtained during quiescence of the system; we therefore presume that the observed spectral broadening is stellar in origin. This then provides a lower limit on the stellar rotational velocity of $v \sin i$=120 km s^{-1}. We can also assume an upper limit from break-up considerations of $v_{\rm rot}$≈190 km s^{-1}.

With these upper and lower bounds on the rotational velocity of V1647 Ori, if we simultaneously push all other measured parameters to their 1 σ limits so as to produce the shortest and longest possible rotation periods, we find with greater than 99.9% confidence that the stellar rotation period lies between 0.6 and 2.7 days. To test the robustness of our calculations, we also calculated the stellar radius using the quiescent V-band extinction and K-band apparent magnitude obtained by Ábrahám et al. [1] prior to the 2004 outburst (∼13 and 10.3 magnitudes, respectively); from this, and assuming an inclination angle of 61° ± 14° as found by Acosta-Pulido et al. [2], we obtain a most likely rotation period of ∼1 d, consistent with the above range. If this is indeed the rotational period of the star, the diurnal gaps in our lightcurve would preclude its detection. In any case, we conclude that the 0.13 d period, and the ∼4 d quasi-periodic modulation, do not correspond to the rotation period of V1647 Ori.

2.3.2 2009 light curve

Figure 2.6 displays our 2009 light curve. The dataset was obtained at very high cadence (~ 10 hr^{-1}) over a timespan of several hours on a single night and, thus, is sensitive only to high frequency variations. A simple χ^2 test shows the light curve to be variable, with reduced $\chi^2_\nu = 10.0$. However, applying the same periodicity analysis as above, we find no significant periodicity in this light curve across the frequency range to which we are sensitive, from 7 d^{-1} to 135 d^{-1}; the strongest peak we obtain has a FAP of 41%.

The full duration of the 2009 light curve is (coincidentally) 0.13 d (7.7 d^{-1}), and thus can be used to check for the presence of a 0.13 d period during the 2009 observations. As shown in Fig. 2.6, a 0.13 d period such as that observed in the 2003 light curve (Fig. 2.4b) is not present in the 2009 light curve. As an additional check, we injected a 0.13 d sinusoid of varying amplitude into these data and found that we were able to induce a significant peak in the power spectrum (FAP $< 1\%$) only if the amplitude of the sinusoid is larger than 0.027 mag. We thus conclude that there is no evidence for an 0.13 d period in the 2009 data with an amplitude greater than 0.027 mag, and we can definitively rule out an 0.13 d signal with an amplitude of 0.05 mag as seen in the 2003–2004 outburst light curve (Fig. 2.2). To summarize, we find that this 2009 lightcurve is variable, but no periodic phenomenon with a frequency in the range to which we are sensitive (7 d^{-1} to 135 d^{-1}) is driving this variability.

In Fig. 2.3 we show the power spectrum of the 2009 light curve data together with that from the 2003 data. The two datasets sample a mostly disjoint range of

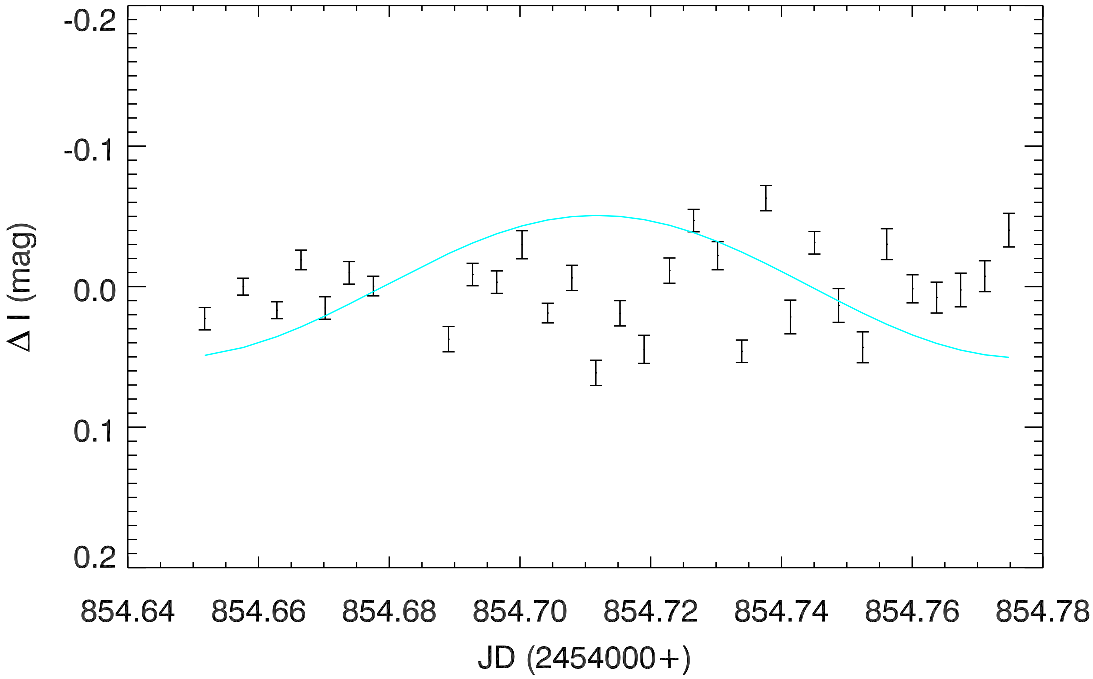

Figure 2.6: Lightcurve of V1647 Ori during 2008–2009 outburst, spanning 0.13 d. These data were taken after the object had reached maximum brightness. No obvious periodic brightness variations are evident. The best-fit 0.13 d sinusoid observed in the 2003 outburst data (Fig. 2.4b) is overplotted here for comparison.

temporal frequencies. However, the two power spectra together are consistent with a single $1/\sqrt{f}$ behavior for the power spectrum as a whole. We suggest one possible interpretation for this $1/\sqrt{f}$ behavior below (Sec. 2.4.2). The only clearly evident difference between the 2003 and 2009 power spectra is in the overlap region near $f = 10$ d^{-1}; as discussed above the 2003 light curve exhibits a strong 0.13 d period whereas the 2009 light curve does not.

2.4 DISCUSSION

We have found strong evidence to suggest that V1647 Ori exhibited a highly significant 0.13 d periodicity in brightness during the rapid brightening phase of its 2003 outburst. The amplitude of this periodic variation was ~0.05 mag. The presence of this feature in the 2003 data, obtained while the object was in the brightening phase, and its absence in the 2009 data, obtained after V1647 Ori had peaked in brightness, suggest that this phenomenon, whatever its cause, is associated with the unstable period of time when the brightness of V1647 Ori was most rapidly increasing. We have also found evidence for a $1/\sqrt{f}$ slope in the power spectrum of V1647 Ori over a large range of temporal frequencies, $0.1 < f < 135$ d^{-1}.

In this section, we consider whether the 0.13 d period may be ascribed to short-lived stellar pulsations, perhaps triggered by the high accretion rate event. Next, we discuss "flickering" in the light curve, evidenced by the $1/\sqrt{f}$ slope in the power spectrum, in the context of a magnetically channeled accretion flow. Finally, we consider whether oscillations originating in the accretion disk, similar to those observed during cataclysmic variable (CV) star outbursts, could be observed in young star outbursts, including FUor and EXor events, and we speculate that the ~4 d quasi-periodic modulation observed in the 2003 light curve could correspond to such an oscillation. The consideration of these mechanisms here is speculative; our aim is to examine whether these explanations may be plausible, but we cannot yet establish that these are definitive driving mechanisms for the observed variability.

2.4.1 Stellar pulsations

Since it is inconsistent with the likely rotation period of V1647 Ori (Sec. 2.3.1.3), we explore the possibility that the 0.13 d period might be a manifestation of pulsation. Given its effective temperature and estimated mass of 0.8 ± 0.2 $M_{\odot}$ [9], and based on comparison with stellar evolutionary tracks [44], we find that V1647 Ori may lie just within the theoretically predicted deuterium instability strip. The expected fundamental mode pulsation period would be approximately 0.5 d [e.g., 131], somewhat longer than the period we detect. In addition, the 0.13 d period does not appear in the 2009 data. It is extremely unlikely that V1647 Ori transitioned from being within the instability strip to being outside the instability strip between our 2003 and 2009 observations.

We next consider whether the dramatic increase in the accretion rate could have induced short term radial oscillations of the stellar surface. From the idealized homogeneous compressible model presented by Cox [41], the period of oscillation, for purely radial pulsation, varies according to

$$\frac{4\pi^2 R^3}{P^2 G M} = -4 + \Gamma_1(2n^2 + 5n + 3) \tag{2.1}$$

where R is the star's radius, P is its pulsational period, G is the gravitational constant, M is the stellar mass, Γ_1 the adiabatic exponent, and n the pulsational mode. For our purposes here, this idealized model is not significantly different from more sophisticated models [130]. Adopting the stellar parameters of V1647 Ori (see Sec. 2.3.1.3) and making the extreme assumption that no part of the star is ionized ($\Gamma_1 = \frac{5}{3}$), we find that the 0.13 d period could correspond to pulsational modes ranging from 2.8 to 4.7. In order to determine the effect of ionization zones on our results, we looked at the extreme case of a fully ionized gas ($\Gamma_1 = \frac{4}{3}$); in this case we find pulsational modes between 3.3 and 5.4. Hence, any errors in not taking ionization zones into account do not significantly change our results. We therefore infer that the 0.13 d period most likely corresponds to a radial pulsation in the 4^{th} oscillation mode, but the 3^{rd} and 5^{th} modes are also permitted within the observational uncertainties in the stellar properties of V1647 Ori.

Pulsation solely in a higher overtone radial mode, although rare, is strongly dependent on the location of the driving mechanism [85]. Examples of similar short-term oscillation-producing phenomena include recent solar observations [77] that revealed that energetic magnetic reconnection and coronal mass ejection events can induce short-lived high-frequency oscillations of the solar surface. In the Sun, these are confined to the vicinity of the triggering event [e.g., 80]. The triggering of radial oscillations by the sudden onset of highly energetic accretion on V1647 Ori thus provides one possible explanation for the observed variability.

2.4.2 Flickering

Flickering is defined as random, small amplitude brightness variations recurring on dynamical timescales [79]. Sometimes interpreted as an observable consequence of an inhomogeneous accretion flow, flickering has been observed in CV stars and, as it is associated with accretion, could be observable during similar outburst events in young stars. Indeed, Kenyon et al. [79] and Rucinski et al. [113] observed flickering in the lightcurves of FU Ori and TW Hya, respectively, the latter through observation of a $1/\sqrt{f}$ slope in the power spectrum. The combination of a high observing cadence and a relatively long time baseline means that our data are sensitive to a large range of frequencies, and, as such, any signs of this phenomenon should be readily apparent in an analysis of the power spectrum of our data.

As discussed in Sec. 4.3, the overall power spectrum of the observed phases of the 2003–2004 and 2008–2009 outbursts of V1647 Ori follow a $1/\sqrt{f}$ trend (Fig. 2.3), which suggests that flickering is one possible origin of the random variability components of the light curve.

The nature of such "flicker noise" is not entirely understood; however, it appears to be linked to situations in which a flow (in this case the accretion of material from disk to star) is funneled or is in some way forced to pass through a physically confined region [107]. Indeed, accretion in young low-mass stars is typically envisioned to occur via magnetospheric funneling of disk material along stellar field lines that thread the inner accretion disk [e.g. 122]. Also, the flickering observed in the CV system T CrB, for example, has been attributed to turbulence in the inner regions of the accretion disk [45]. Thus the observation of flickering in V1647 Ori might suggest an interaction between the stellar magnetosphere and the inner regions of the accretion disk during outburst, with material continuing to accrete onto the star along stellar magnetic field lines [e.g. 122].

2.4.3 Dwarf Nova-Like Oscillations in the Keplerian Inner Accretion Disk?

We have observed a modulation with a timescale of ∼4 d in the 2003 light curve of V1647 Ori (Fig. 2.2). As discussed, our data do not permit us to determine whether this modulation is strictly periodic, or indeed whether it persists for more than ∼2 cycles. It is nonetheless a potentially interesting quasi-period that could arise in a number of different ways.

Dwarf-nova oscillations (DNOs) are quasi-periodic brightness variations typically observed in cataclysmic variable star outbursts. These phenomena are associated with accretion, and they may persist during quiescence [109]. The oscillations are not observed in all CV outbursts, and the oscillation frequencies may change during a high accretion rate event. Because of their relatively short periods, DNOs are believed to originate at the inner edges of Keplerian accretion disks. They have only rarely been observed during the rise of a CV outburst [139], but their behavior is thought to be well described by a low-inertia magnetic accretor model in which accretion induces variations in the angular velocity of an equatorial accretion belt [140]. In addition, so-called quasi-periodic oscillations (QPOs), which are longer term, less coherent oscillations, have also been observed during some CV outbursts. There is no generally accepted model for what causes the QPO brightness modulations, but they are thought to be accretion disk phenomena [e.g., 141]. In any event, an empirical relationship links DNOs to QPOs such that $P_{\rm QPO} \approx 15 \times P_{\rm DNO}$ [140].

The low-inertia magnetic accretor model predicts that the DNO oscillation quasi-period ($P_{\rm DNO}$) increases as the accretion rate ($\dot{M}$) decreases. It also predicts that

$P_{\rm DNO}$ corresponds to the Keplerian orbital period of the inner edge of the accretion disk. If we assume a $P_{\rm DNO}$–$\dot{M}$ relation such as that found empirically for the dwarf nova SS Cyg by Mauche [92] and use the $\dot{M}$ found for V1647 Ori by Muzerolle et al. [101], we find $P_{\rm DNO} \sim 5.7$ d. We note that the value of $\dot{M}$ might differ for our data, bringing $P_{\rm DNO}$ closer to our observed quasi-period of 4.14 d. For example, using the $P_{\rm DNO}$–$\dot{M}$ relation, we calculate that $\dot{M} \sim 10^{-4}$ $M_\odot$ yr^{-1} would yield a period of 4.2 d. In any event, if this model applies to the V1647 Ori system, then, taking the mass of the central star to be ~ 0.8 $M_\odot$, we calculate that the inner edge of the accretion disk surrounding V1647 Ori was located ~2.5 stellar radii from the star prior to the peak of the outburst. This model could thus suggest that the stellar magnetosphere was still capable of holding off the inner disk, at least during the early stages of the 2003–2004 outburst.

Additionally, using the relation of $P_{\rm QPO} \approx 15 \times P_{\rm DNO}$, we would expect to observe a QPO with a period of ~60 d, which is very close to the 56 d period found by Acosta-Pulido et al. [2] who attributed it to dense circumstellar clumps orbiting the star. However, given the non-uniform sampling of our data and the fact that these oscillations are observed over only ~2 cycles, the reality of this period, and the link between these periodicities and those observed in white dwarf stars, is unclear. Nevertheless, they are potentially intriguing. Observations probing similar timescales during FUor/EXor outbursts would allow us to further investigate the presence of such phenomena in young star outbursts.

2.5 SUMMARY

In this work, we present high cadence time-series photometry of V1647 Orionis during its two most recent outburst events. The overall power spectrum of our 2003 and 2009 datasets displays a $1/\sqrt{f}$ 'flicker noise' spectrum. The detection of 'flicker noise' in the power spectra of our light curves suggests that accretion continues to be mediated by the stellar magnetosphere during the observed phases of the 2003–2004 and 2008–2009 outbursts. This picture is bolstered by the observation of a quasi-periodic modulation in the 2003 light curve with a timescale of $\sim$4 d, perhaps arising from a CV-like quasi-periodic oscillation of the inner accretion disk edge at a height of 2–3 stellar radii from the stellar surface.

Our Fourier analysis of our 2003 detrended lightcurve, obtained mid-outburst, yields a periodic variation on a timescale of 0.13 d that persists in spite of the dramatic rise in brightness caused by the outburst. This period, detected at very high statistical significance, is not attributable to the expected rotation period calculated from other measured properties of the star. This 0.13 d period is absent from our 2009 light curve.

The 0.13 d period is very coherent in the 2003 dataset, and it is therefore likely to have been a truly periodic phenomenon during those observations. Given that we do not detect this period in our 2009 light curve, obtained post-outburst, we conclude that it is probably an accretion-induced process associated with the epoch when the brightness of the object is increasing (and so perhaps when the accretion rate is increasing), one likely candidate being short-lived radial pulsations of the star.

Chapter 3

AN OBSERVATIONAL CORRELATION BETWEEN STELLAR BRIGHTNESS VARIATIONS AND SURFACE GRAVITY

Surface gravity is one of a star's basic properties, but it is difficult to measure accurately, with typical uncertainties of 25-50% if measured spectroscopically [134, 54] and 90-150% photometrically [31]. Asteroseismology measures gravity with an uncertainty of about 2% but is restricted to relatively small samples of bright stars, most of which are giants [36, 70, 126]. The availability of high-precision measurements of brightness variations for >150,000 stars [17, 18] provides an opportunity to investigate whether the variations can be used to determine surface gravities. Granulation power on a star's surface correlates physically with surface gravity [91, 82]; if brightness variations on timescales of hours arise from granulation [29], then such variations should correlate with surface gravity. Here we report an analysis of archival data that reveals an observational correlation between surface gravity and the root-mean-square brightness variations on timescales of less than eight hours for stars with temperatures of 4500-6750 K, surface gravities of 2.5-4.5 dex (cgs), and having overall brightness variations <3 parts per thousand. A straightforward observation of optical brightness variations therefore allows, using this correlation, a determination of the surface gravity with an error of $< 25\%$ for inactive Sun-like stars at main-sequence to giant stages of evolution.

---

[0] A version of this chapter was published in *Nature*, vol. 500, pp427-430 (2013).

Brightness variations of Sun-like stars are driven by many factors, including granulation [56], oscillations [29], rotation, and magnetic activity [129]. As they evolve from high surface gravity (g) dwarfs to low-g giants, their convective zones deepen, they rotate more slowly, their magnetic activity diminishes, and their oscillation and granulation timescales increase, all of which will change the nature of the brightness variations. It has been previously demonstrated that the power in granulation (as traced by the Fourier spectrum of the brightness variations) is inversely proportional to ν_{max}, the peak frequency of Sun-like acoustic oscillations [91, 56]. Given that ν_{max} is itself proportional to g [29], it naturally follows that g should manifest in brightness variations on timescales that trace granulation. Although physically we expect this, it is not immediately apparent that brightness variations can be used as an effective determinant of g because other phenomena not directly related to g–most importantly spots, plages, and other sources of brightness variations driven by the star's magnetic activity–likely dominate the observed brightness variations. It is necessary therefore to filter out the brightness variations arising from these phenomena, which generally occur on timescales of hours to days, while preserving the brightness variations related to granulation and g on timescales of minutes to hours.

Using long cadence (30 minute) light curves from Quarter 9 of NASA's Kepler Mission [25], we observe clear patterns in the evolutionary properties of stars encoded in three simple measures of their brightness variations [18] (Fig. 3.1): Range ($\mathrm{R_{var}}$), number of zero crossings (X_0), and root-mean-square on timescales shorter than 8 hours (to which we refer hereafter as "8-hr flicker," or simply F_8). Relating these measures to g determined asteroseismically for a sample of Kepler stars [35], we find distinctive features that highlight the way stars evolve in this three-dimensional space, making up an evolutionary diagram of photometric variability. Within this diagram we find a vertical cloud of points, largely made up of high-g dwarfs, that show large $\mathrm{R}_{\mathrm{var}}$, small X_0, and low F_8. Most strikingly, we observe a tight sequence of stars–a "flicker floor" sequence that defines a dramatically protruding lower envelope in $\mathrm{R}_{\mathrm{var}}$–spanning gravities from dwarfs to giants. Sun-like stars of all evolutionary states evidently move onto this sequence only when they have a large X_0, which in turn implies low stellar activity.

Remarkably, we find that g is uniquely encoded in F_8, yielding a tight correlation between the two (Fig. 3.2). Moreover, using 11 years of SOHO Virgo [51, 19] light curves of the Sun and sampling them at the same cadence as the Kepler long-cadence light curves, we find that the Sun's (constant) g also manifests in this metric, which remains invariant throughout the 11-year solar activity cycle even while the Sun's $\mathrm{R}_{\mathrm{var}}$ and X_0 change significantly from the spot-dominated solar maximum to the nearly spotless solar minimum. From the Sun's behavior we infer that a significant portion of the vertical scatter of the Kepler stars within the vertical cloud at the left of the diagram may be driven by solar-type cyclic activity variations. Most importantly, the Sun's true g fits easily on our empirical relation, and the g of any Sun-like Kepler star from dwarf to giant may be inferred from this relation with an accuracy of 0.06-0.10 dex (see Supplementary Information for more details).

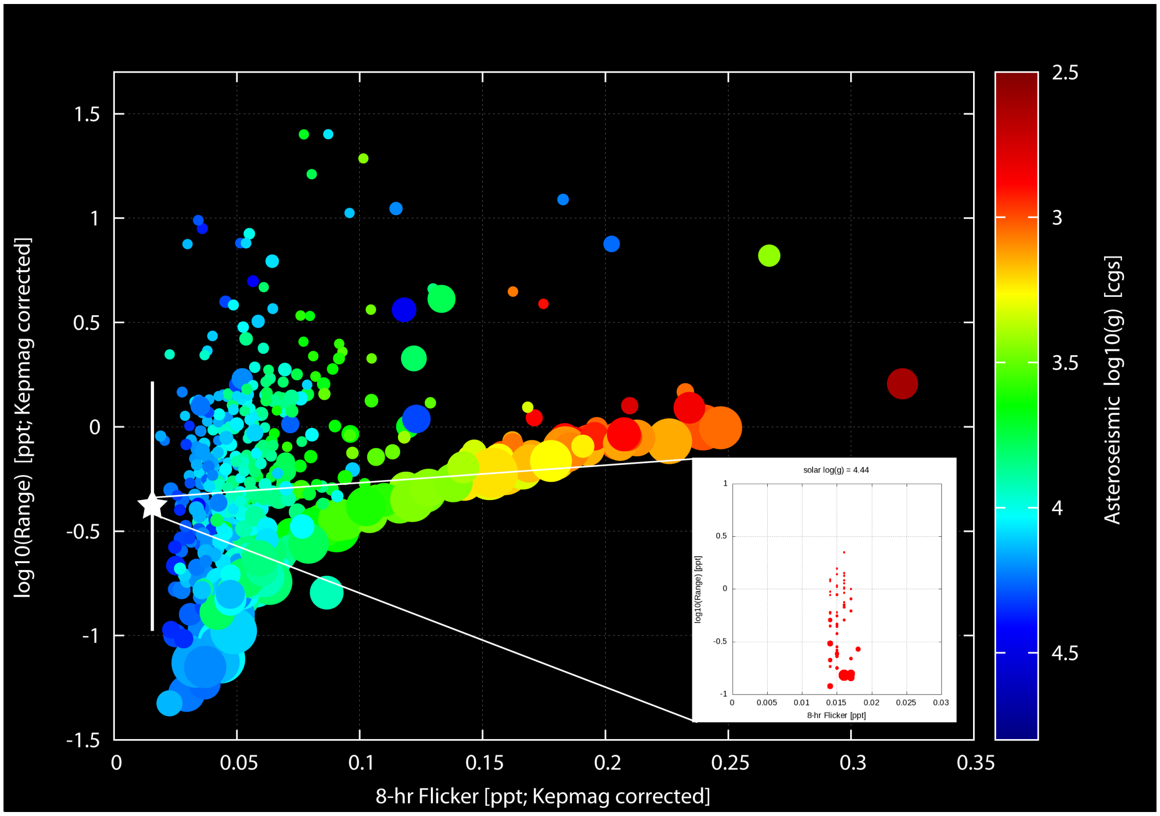

Figure 3.1: Simple measures of brightness variations reveal a fundamental "flicker sequence" of stellar evolution. We establish the evolutionary states of stars with three simple measures of brightness variations [18]. The abscissa, 8-hr flicker (F_8), measures brightness variations on timescales of 8 hours or less and is measured in units of parts per thousand ("ppt"). The ordinate, $\mathrm{R}_{\mathrm{var}}$, yields the largest amplitude of the photometric variations in a 90-day timeframe. X_0 (symbol size; ranging from 0.01 to 2.1 crossings per day), conveys the large-scale complexity of the light curve. We correct both $\mathrm{R}_{\mathrm{var}}$ and F_8 for their dependence on Kepler magnitude ("Kepmag"). Color represents asteroseismically determined g. We observe two populations of stars: a vertical cloud composed of high-g dwarfs and some subgiants, and a tight sequence, the flicker floor, spanning an extent in g from dwarfs to giants. The typically large $\mathrm{R}_{\mathrm{var}}$ of stars in the cloud, coupled with their simpler light curves (small X_0), implies brightness variations driven by rotational modulation of spots. In contrast, large X_0 characterizes stars on the sequence. The F_8 of stars in this sequence increases inversely with g because its physical source is sensitive to g. $\mathrm{R}_{\mathrm{var}}$ also increases with F_8 along the floor, because F_8 is a primary contributor to $\mathrm{R}_{\mathrm{var}}$ (as opposed to starspots above the floor). Stars with a given F_8 cannot have $\mathrm{R}_{\mathrm{var}}$ below that implied by F_8 itself: quiet stars pile up on the flicker floor because they are prevented from going below it by the statistical definition of the two quantities. Stars above the floor have larger amplitude variations at longer timescales that set $\mathrm{R}_{\mathrm{var}}$. The large star symbol with vertical bars and the inset show the Sun's behavior over the course of its 11-year magnetic cycle. The Sun's F_8 is largely invariant over the course of its cycle, just as its g is invariant.

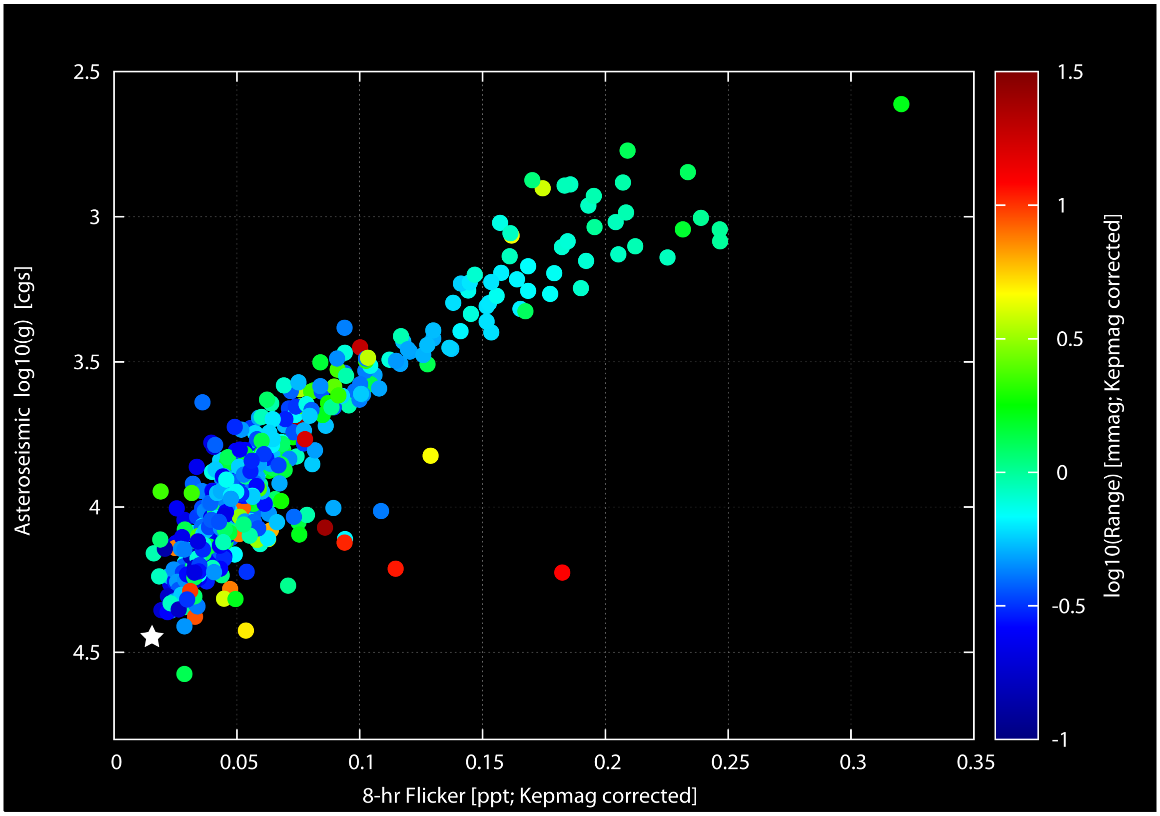

Figure 3.2: Stellar surface gravity manifests in a simple measure of brightness variations. The same stars from Fig. 3.1 with Kepler Quarter 9 data are shown. Asteroseismically determined [36] g shows a tight correlation with F_8. Color represents the $\mathrm{R}_{\mathrm{var}}$ of the stars' brightness variations; outliers tend to have large brightness variations. Excluding these outliers, a cubic polynomial fit through the Kepler stars and through the Sun (large star symbol) shows a median absolute deviation of 0.06 dex and a root-mean-square deviation of 0.10 dex (see the Supplementary Information). In order to simulate how the solar g would appear in the archival data we use to measure g for other stars, we divide the solar data into 90-day "quarters." Our F_8-g relation measured over multiple quarters then yields a median solar g of 4.442 with a median absolute deviation of 0.05 dex and an RMS error of 0.009 dex (the true solar g is 4.438).

Asteroseismic analyses derive g from the properties of stellar acoustic oscillations [36, 30, 38, 37]. Given that near-surface convection drives both these oscillations and granulation, and given the brightness variability timescales to which F_8 is sensitive, we suggest that a combination of different types of granulation (with typical solar timescales from ~30 minutes to ~30 hours [46]) drives g's manifestation in this metric. The precise timescales of these phenomena in solar-type stars depend strongly on the stellar evolutionary state and hence also on g [70, 91, 82, 81]. Acoustic oscillations, whose amplitudes are sensitive to g [70], may provide an increasingly important contribution to F_8 as stars evolve into subgiants and giants and the amplitudes and timescales of these oscillations increase [70, 91, 82]. At some point, the p-mode and granulation timescales cross [91], which may lead to a breakdown of our F_8-g relation at very low g.

Using F_8 to measure g, we can construct a photometric variability evolutionary diagram for most stars observed by Kepler, even for stars well beyond the reach of asteroseismic and spectroscopic analysis (Fig. 3.3). Coding this diagram by the stars' temperatures and rotation periods, we may trace the physical evolution of Sun-like stars as follows: stars begin as main-sequence dwarfs with large photometric $\mathrm{R_{var}}$ and a small X_0, presumably driven by simple rotational modulation of spots at relatively short rotation periods. As they spin down to longer rotation periods, the stars' brightness variations become steadily "quieter" (systematically lower $\mathrm{R_{var}}$), but then become suddenly and significantly more complex (larger X_0) as they land on the "flicker floor." Some stars alight onto the floor only after beginning their evolution as low-g subgiants, having moved to the right (higher F_8) as their effective temperatures begin rapidly dropping. Other stars join the sequence while still dwarfs, easily identified in our diagram by the dramatically increased X_0 at very low F_8. Evidently some dwarf stars become magnetically quiet while still firmly on the main sequence, whereas others do not reach the floor until they begin to swell significantly. Interestingly, the Sun appears to approach the flicker floor at solar minimum; its $\mathrm{R_{var}}$ becomes quite low and its X_0 strongly increases (Fig. 3.1).

A star's main-sequence mass and initial spin likely determine where along the flicker floor sequence it ultimately sets down, as a star's motion downward and rightward in our diagram is essentially a competition between its spin-down and structural evolutionary timescales, respectively. Regardless, once on the floor all stars evolve along this sequence and stay on it as they move up to the red giant branch, their effective temperatures steadily dropping as their surfaces rapidly expand. Despite their very slow rotation as subgiants and giants on the flicker floor sequence, their photometric $\mathrm{R_{var}}$ is steadily driven upwards by the increasing F_8 that reflects the stars' continually decreasing g. The increasing $\mathrm{R_{var}}$ and F_8 of subgiants and giants on the flicker floor is likely the result of the increasingly important contribution of radial and non-radial pulsations to the overall brightness variations [62, 55].

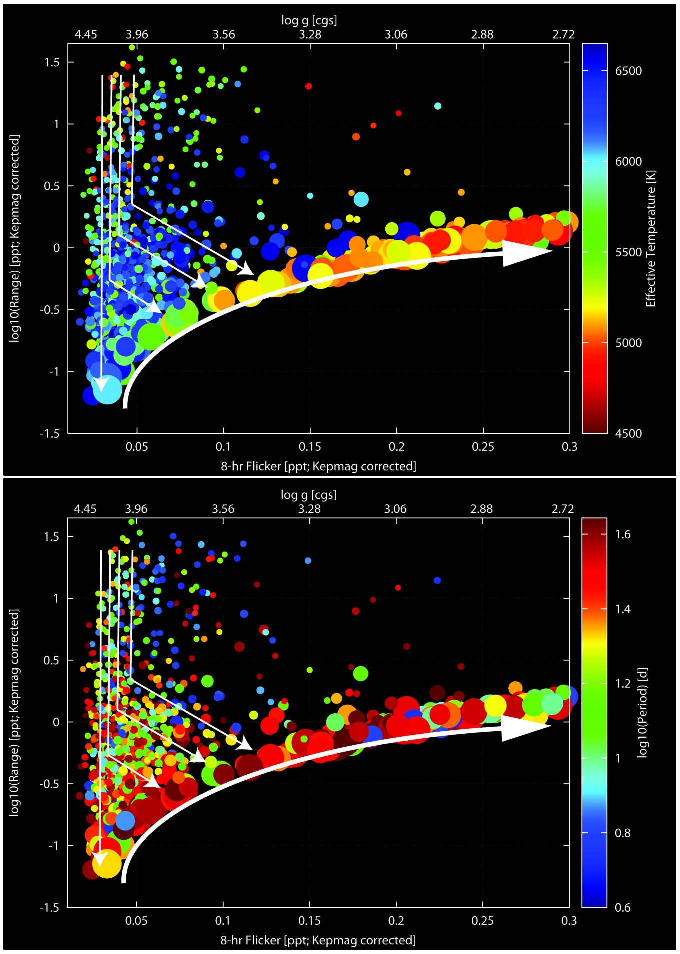

Figure 3.3: An integrative view of stellar evolution in a new diagram of brightness variations. Same as Figure 3.1 but for Kepler stars lacking asteroseismic g. We include a g scale at the top (from conversion of the F_8 scale at bottom via our calibrated relationship). Here, we selected stars with Kepler magnitudes between 11.0 and 11.85 in order to limit the sample to 1000 stars for visual clarity (1,012 points are shown). We removed objects that are potentially blended (Kepler flux contamination greater than 0.05) as well as those that may be galaxies (Kepler star-galaxy flag other than 0). Arrows qualitatively indicate the evolutionary paths of Sun-like stars in this diagram. Stars generally move from top to bottom, as the overall brightness fluctuations due to spots decrease with time, and then from left to right as their g decreases. All stars eventually arrive on the flicker floor sequence and evolve along it. *Left*: Color represents effective temperature. Stars clearly cool as they evolve from left to right, from dwarfs to red giants. We restricted the effective temperatures to be 4500-6650 K, using the revised temperature scale for Kepler stars [105]. *Right*: Same as left, but color-coded by the dominant periodicity in the light curve. We limited the sample to stars with dominant periods longer than 3 days (to eliminate very rapidly rotating active stars) and shorter than 45 days (half the Kepler 90-day data interval). This period traces rotation for unevolved stars and pulsations for evolved ones. Dwarfs generally show the expected spin-down sequence with decreasing R_{var} (correlated with the level of surface magnetic activity). Subgiants and giants broadly display very slow rotation as expected.

A few stars appear as outliers to the basic picture we have presented here, seen toward the right of the vertical cloud of points in our evolutionary diagram (Fig. 3.3). Some active dwarfs have higher F_8 than expected for their g. Frequent strong flares can boost F_8 as currently defined, and some hotter dwarfs are pulsators with enough power near 8 hours to elevate their F_8. A few such cases appear also in the asteroseismic sample (Fig. 3.1). Some lower g stars have $\mathrm{R_{var}}$ above the flicker floor due to the presence of magnetic activity [121], slow radial pulsations or secular drifts. Finally, a few outliers are simply due to data anomalies. As our technique is refined, these exceptions should be treated carefully before assigning a F_8-based g, particularly for high-F_8 stars with $\mathrm{R_{var}}$ above $\sim$3ppt. They constitute a small fraction of the bulk sample, and most of them can be identified as one of the above cases.

Common to all of the stars along the flicker floor is the virtual absence of spot activity as compared to their higher $\mathrm{R_{var}}$ counterparts; short-timescale phenomena such as granulation and oscillations dominate the brightness variations. Given that spots likely suppress acoustic oscillations in the Sun and other dwarf stars [70, 34, 83, 35], the large X_0 of stars along this sequence may partially reflect the ability of short-timescale processes to manifest more strongly now that large spots no longer impede them, along with the changing convective patterns. As the stars become full-fledged red giants and beyond, the principal periodicity in their brightness variations increasingly reflects shorter-period oscillations, as opposed to their inherently long-period rotation, as oscillations become dominant over magnetic spots.

It may be possible to differentiate between stars with similar g but different internal structures (e.g., first-ascent red giants versus helium burning giants) through application of a sliding timescale of F_8 as a function of g, where the sliding timescale would capture the changing physical granulation timescales with evolutionary state [37]. Moreover, the behavior of stars on the flicker floor may explain the source of radial velocity "jitter" that now hampers planet detection through radial velocity measurements [21].

3.1 Supplementary Information

3.1.1 Asteroseismic measurement of surface gravities (g)

We used as our sample the first ensemble asteroseismic analysis of Kepler stars [35]. The $\Delta\nu$ and ν_{max} values from that work were shared with us privately by the authors (D. Huber and T. Metcalfe, priv. comm.). ν_{max} refers to the central frequency of the solar-like p-mode oscillations, where the power is greatest, while $\Delta\nu$, the large frequency separation, measures the sound travel time across the star's diameter [37]. Taking these, together with the revised stellar effective temperatures [105], we applied the standard scaling relations that transform them into mass and radius [35] to calculate g. Seismic parameters are now available for several thousand stars [70, 37] and will be used in a future calibration of our F_8-g relation.

3.1.2 Detailed description of how each of the photometric variability measures is calculated

We employ the following three variability statistics [18] in this work. We use as our starting point for all of these Kepler Quarter 9 PDC-MAP data:

Range (R_{var}): obtained by sorting the pipeline-reduced Kepler light curve by differential intensity and measuring the range between the 5th and 95th percentile. This quantity traces the stellar surface spot coverage. Number of zero crossings (X_0): computed by smoothing the light curve by 10 hour (20 point) bins and counting the number of times the resultant light curve crosses its median value. It provides an assessment of the complexity of the light curve. For example, spots produce variations larger than the high-frequency noise resulting in a small X_0

8-hour flicker (F_8): determined by performing a 16-point (8 hour) boxcar smoothing of the light curve, subtracting it from the original light curve and measuring the root-mean-square (RMS) of the result. We handle data gaps by interpolating across any missing 30-minute data bins. The result is a somewhat decreased F_8 because it is zero in these interpolated segments. In practice the data gaps are so few and small that the impact on the overall F_8 is negligible. We, at present, do not employ sigma-clipping. There are rare cases in which a few light curve points are extreme enough to boost the RMS, but are clipped from the R_{var}. Such cases can appear below the "flicker floor" we have described. Examples include a quiet star with a deep transiting planet, or one very large instrumental spike affecting only a few points. F_8 measures stellar variability on timescales of 8 hours or less.

3.1.3 Details on how the solar data were put into "Kepler equivalent" form

We used SOHO Virgo [51] light curves, whose passband is similar to that of Kepler [19]. We took light curves spanning an entire solar cycle to examine the influence of changing spot activity (i.e. changing R_{var}) over the course of a stellar magnetic cycle on our findings. We divided the SOHO light curve into 90 day segments, to simulate the length of a Kepler “quarter,” and we sampled each segment to achieve an effective cadence of 30 minutes, similar to the cadence of the Kepler long-cadence light curves. We note that the actual derived F_8 depends on the filter used and the treatment of the solar data. The solar brightness variations are largest in the blue filter, moderate in the green filter, and smallest in the red filter (as expected for the temperature of the Sun). One finds, for instance, a roughly 30% larger F_8 than the value reported here when considering solely the green filter data. Thus, previous analyses have used a sum of the green and red filter data (which is more nearly the same as a broadband filter), and we now use the TSI “white” data (which is also a broadband realization of the solar variations).

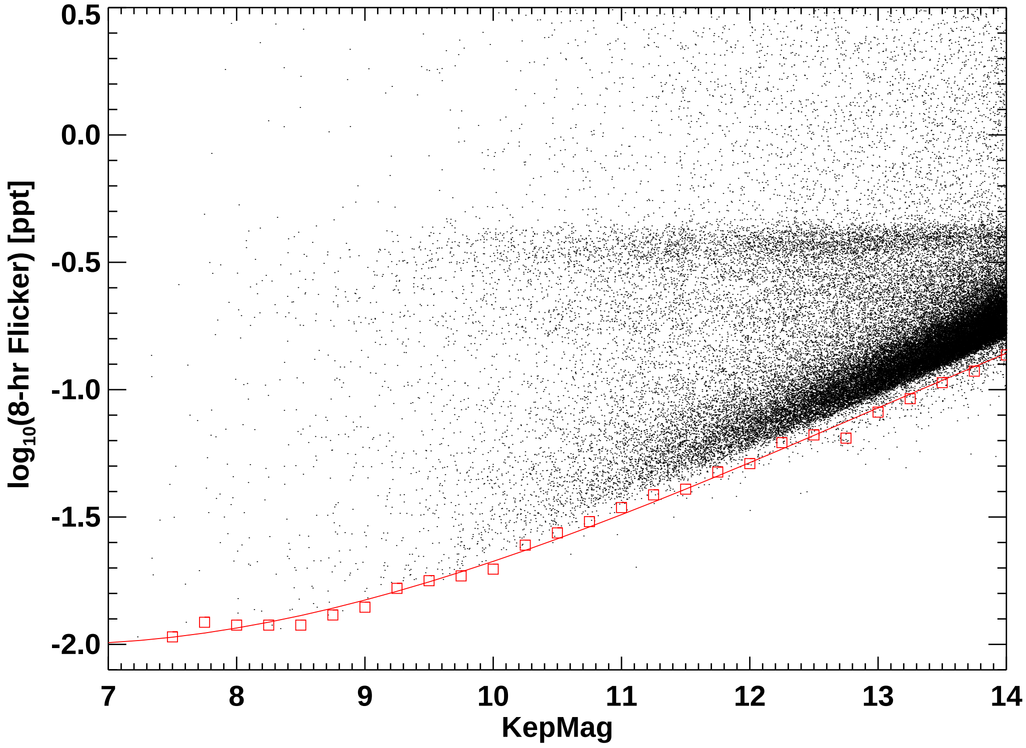

Figure 3.4: Kepler Magnitude correction: The measures of brightness variations that we use all show dependencies on stellar brightness. Fainter stars naturally exhibit larger brightness variability in $\mathrm{R_{var}}$ and F_8 simply due to increased photon noise. Not accounting for this results in an overestimate of F_8 (equivalently, an underestimate of g). We therefore correct these measures using empirical relations obtained from the entire sample of Kepler Quarter 9 light curves. We fit each of the brightness variability measures versus stellar apparent magnitude in the Kepler bandpass ("Kepmag" or K_p) using a simple 4th order polynomial fit to the lower envelope of points, defined as the bottom 0.5-th percentile of points in 0.1 magnitude wide bins. These polynomial relations were then subtracted in quadrature from the measured brightness variation measures, and these corrected variability measures are identified in all figures as "Kepmag corrected." The final Kepler magnitude relation used in this work is: $min(log_{10}F_8) = -0.03910 - 0.67187K_p + 0.06839K_p^2 - 0.001755K_p^3$ where K_p is the Kepler magnitude, and the fit applies for $7 < K_p < 14$. The final F_8 that we use is obtained by subtracting this min(F_8) from the measured F_8 in quadrature (the quadrature subtraction is performed linearly, not logarithmically).

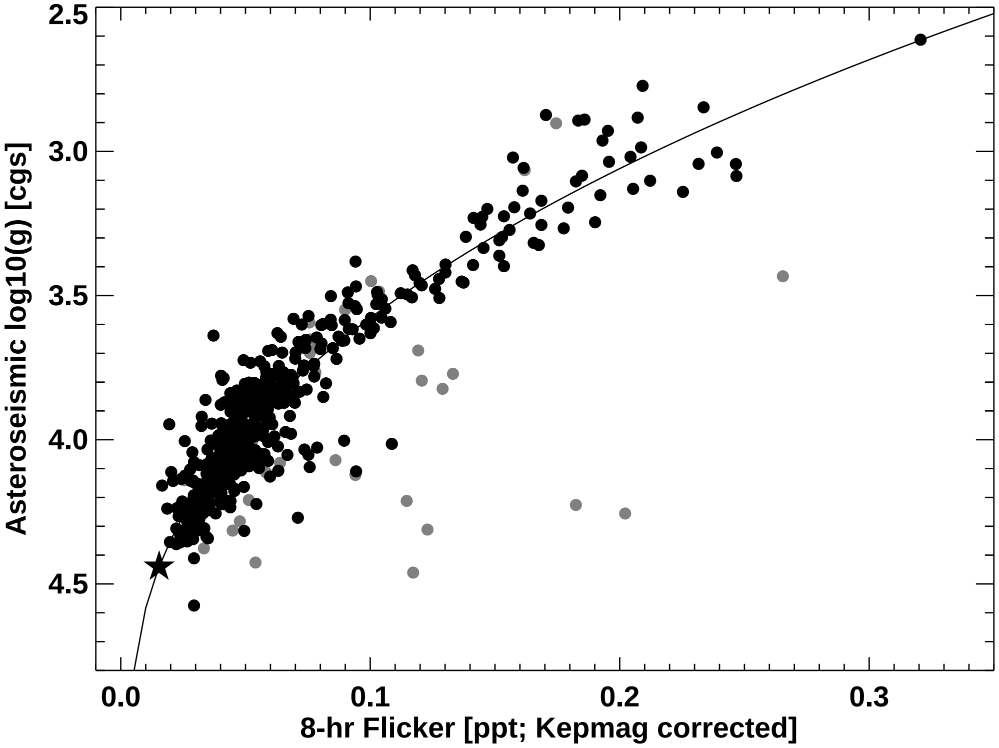

Figure 3.5: Details on g versus F_8 fit relation: We draw our "gold standard" sample from the first published asteroseismic analysis of Kepler stars [36] (we note that there are now over 10,000 seismically analyzed Kepler stars that will permit our relations to be extended further in future work). From these, we used as our base sample the 542 stars (gray points) possessing both asteroseismically determined masses and radii and Quarter 9 long-cadence light curves from which we could compute our variability statistics [18]. These stars have Kepler magnitudes brighter than 12, effective temperatures [105] between 4500 < Teff < 6650 K, and a Kepler flux contamination flag of less than 0.05. Most of the outliers from the trend are stars with very short periods (likely short-period pulsators or rapidly rotating active stars) and/or large brightness excursions (R_{var}). Therefore, we removed from the polynomial fit 10 stars with Period < 3 days and 19 additional stars with $R_{\mathrm{var}} > 2.5$ ppt. The remaining 503 stars (black) were fitted with a cubic polynomial (solid curve). F_8 was corrected for the dependence on Kepler magnitude as above. The large star symbol at lower left represents the Sun with $g = 4.44$ and a median F_8 of 0.015 ppt over the entire 11-year solar activity cycle. The polynomial fit was forced through the solar value since there are few asteroseismic stars with g as high as the Sun, however the fit passes within 0.05 dex of the solar value even without forcing the fit. The final polynomial fit relation is: $log_{10} g = 1.15136 - 3.59637x - 1.40002x^2 - 0.22993x^3$ where x = $log_{10}(F_8)$ and F_8 is in units of ppt. The root-mean-square of the g residuals about the polynomial fit is 0.10 dex and the median absolute deviation is 0.06 dex.

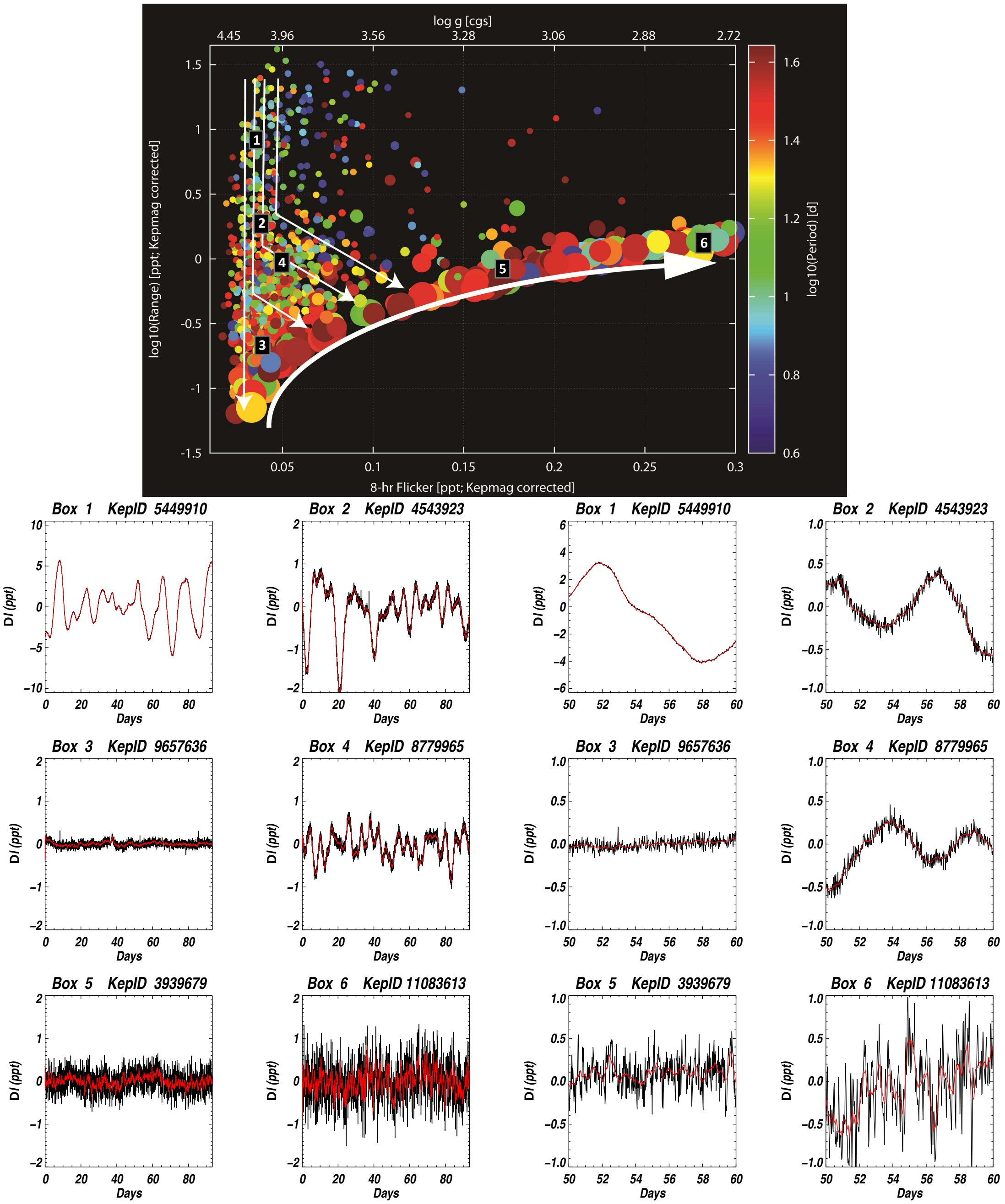
log g [cgs]
4.45
3.96
3.56
3.28
3.06
2.88
2.72
1.5
1
0.5
0
-0.5
-1
-1.5
0.05
0.1
0.15
0.2
0.25
0.3
8-hr Flicker [ppt; Kepmag corrected]
log10(Range) [ppt; Kepmag corrected]
log10(Period) [d]
1.6
1.4
1.2
1
0.8
0.6
1
2
3
4
5
6
Box 1 KepID 5449910
Box 2 KepID 4543923
Box 3 KepID 9657636
Box 4 KepID 8779965
Box 5 KepID 3939679
Box 6 KepID 11083613
DI (ppt)
Days
0
20
40
60
80
50
52
54
56
58
60
10
5
-5
-10
2
-1
-2
6
4
-4
-6
1.0
0.5
0.0
-0.5
-1.0

Figure 3.5: Examples of light curves in different regions of the photometric variability evolutionary diagram: *Top*: The photometric evolutionary diagram, showing the regions from which we draw our sample light curves. *Bottom Left*: Six examples of light curves from Quarter 9 with different $\mathrm{R}_{\mathrm{var}}$ and F_8. The black curves show the differential intensity in units of parts per thousand. The red curves show the result of applying a boxcar smoothing of 16 points (8 hours). Thus, the F_8 is the RMS difference between the black and red curves. The first three stars are taken from the left hand edge of Figure 3.5, *top*, at the top, middle, and bottom of the dwarf stars (labeled 1-3). Though most stars in this region are likely dwarfs, a small fraction of giants with very low g (typically also with very large $\mathrm{R}_{\mathrm{var}}$) contaminate this region. One could enhance the determination of g for dwarfs with $\mathrm{R}_{\mathrm{var}} > 2.5$ ppt by considering additional diagnostics present in the same light curve data. For example, the true dwarfs that dominate the upper left part of the diagram have large $\mathrm{R}_{\mathrm{var}}$ and are therefore active. They thus should exhibit strong periodicity on timescales expected for rotation of active dwarfs (i.e., Prot $<$ 20 d). The second set of three stars are at evenly spaced locations along the flicker floor in that figure, moving out to higher F_8 and $\mathrm{R}_{\mathrm{var}}$ (labeled 4-6). The Kepler IDs of each star are indicated. *Bottom Right*: A 10-day section of the light curves, to bring out more details. The $\mathrm{R}_{\mathrm{var}}$ and F_8 values for the six stars are listed here also for reference (cf. Table 3.1). We also include the temperatures [105] and the g from both the Kepler Input Catalog and our F_8 relation.

Table 3.1. Fundamental Parameters of Sample Stars

Star	Kepler ID	Effective Temperature[a]	Kepler Magnitude	R_{var}	F_8	Magnitude-corrected F_8	g (cgs) from KIC	g (cgs) from F_8
1	5449910	5417	11.235	8.561	0.046	0.029	4.539	4.212
2	4543923	6062	11.623	1.841	0.055	0.034	4.248	4.141
3	9657636	6153	11.253	0.206	0.049	0.033	4.209	4.155
4	8779965	5799	11.730	0.956	0.067	0.049	3.578	3.974
5	3939679	5036	11.099	0.707	0.171	0.171	4.248	3.191
6	11083613	5062	11.629	1.359	0.284	0.284	3.361	2.738

[a] From [105]

Chapter 4

RADIAL VELOCITY VARIATIONS OF PHOTOMETRICALLY QUIET, CHROMOSPHERICALLY INACTIVE *KEPLER* STARS: A LINK BETWEEN RV JITTER AND PHOTOMETRIC FLICKER

We compare stellar photometric variability, as measured from *Kepler* light curves by Basri et al. [18], with measurements of radial velocity (RV) root-mean-square (RMS) variations of all California Planet Search overlap stars. We newly derive rotation periods from the Kepler light curves for all of the stars in our study sample. The RV variations reported herein range from less than 4 m s^{-1} to 135 m s^{-1}, yet the stars all have amplitudes of photometric variability less than 3 mmag, reflecting the preference of the RV program for chromospherically "quiet" stars. Despite the small size of our sample, we find with high statistical significance that the RV RMS manifests strongly in the Fourier power spectrum of the light curve: stars that are noisier in RV have a greater number of frequency components in the light curve. We also find that spot models of the observed light curves systematically underpredict the observed RV variations by factors of ∼2–1000, likely because the low level photometric variations in our sample are driven by processes not included in simple spot models. The stars best fit by these models tend to have simpler light curves, dominated by a single relatively high amplitude component of variability. Finally, we demonstrate that the RV RMS behavior of our sample can be explained in the context of the photometric variability evolutionary diagram introduced by Bastien et al. [20]. We

---

[0] A version of this chapter was published in *The Astronomical Journal*, vol. 147, pp29-39 (2014).

use this diagram to derive the surface gravities of the stars in our sample, revealing many of them to have moved off the main-sequence. More generally, we find that the stars with the largest RV RMS are those that have evolved onto the "flicker floor" sequence in that diagram, characterized by relatively low amplitude but highly complex photometric variations which grow as the stars evolve to become subgiants.

4.1 INTRODUCTION

An outstanding problem in the detection of planets via either the transit or radial velocity (RV) methods is noise caused by stellar magnetic activity. Manifestations of this activity, such as starspots, convective turbulence, and granulation, can impede, and sometimes even mimic the signals that planets produce, particularly low-mass, Earth-like ones. Photometric and RV characterizations of this activity are therefore of great importance and have been the subject of a number of studies (see, e.g., Pont et al. [106], Saar et al. [116], and Wright [143]).

RV noise, or "jitter," is a particularly pernicious problem that has resulted in false detections [103] and complicated the confirmation of transiting planets [13, 60]. Attempts to study the impact of stellar processes on our ability to detect planets include Dumusque et al. [46, 47], who simulate the effects of granulation and starspots, respectively, on RV measurements, and Saar [118], who semi-empirically models the effect of plages on RV observations of G dwarfs. Empirical studies include that of Wright [143] which, employing a large sample of stars observed as part of the California and Carnegie Planet Search program, provides a relationship linking the magnitude of RV jitter with the $B-V$ color and absolute magnitude of a star. A challenge to all studies so far is the finding that the RV jitter can in some cases be "loud" even when the star is chromospherically (and presumably photometrically) very "quiet," indicating that for the some stars the driver of the RV jitter is not manifested as simple photometric variability [72, 143].

Many studies, including those we now describe, have examined the relationships between RV variations and photometric variability. Many of the photometric manifestations of stellar activity, however, occur at the mmag level, which has been largely inaccessible to ground-based studies.

Saar et al. [116], the classic study characterizing the relationship between RV variations and photometric variability, found a correlation between the weighted radial velocity dispersion (corrected for contributions from planetary companions and the mean internal error), the effective temperature, and the stellar rotational velocity. Subsequent works include the examination of correlations with other activity indicators (see, for example, Martínez-Arnáiz et al. [89]). Saar & Donahue [115] employed simple models to examine how RV measurements are affected by starspots and convective inhomogeneities, finding that the amplitude of RV variations is related to starspot area coverage and rotational velocity. They additionally see that convective inhomogeneities manifest in line bisector variations and also depend on rotational velocity and effective temperature. More recently, with the public release of Kepler data, Aigrain et al. [4] propose a model based on distributed starspots to predict the RV jitter of a star from a well-sampled light curve.

Now, with the advent of missions like CoRot [11], MOST [137] and *Kepler* [25], which offer sub-mmag photometric precision over a long time baseline for a multitude of stars, we may re-examine empirical relationships between photometric variability and RV variations. We may now extend the photometric analysis beyond measuring the rotation period, using different ways of characterizing the light curves and examining how these characterizations relate to activity and RV variability. Importantly, we may now examine the causes of RV jitter at very photometric variability levels, and thus hope to resolve the mystery of RV jitter in otherwise "quiet" stars.

Indeed, in an initial ensemble examination of the *Kepler* light curves, Basri et al. [18] find a wide variety in the photometric behavior of Sun-like stars, notably including temporally coherent but non-periodic variability and highlighting the *Kepler* Mission's sensitivity not only to stellar spots but also very low-level phenomena (see also McQuillan et al. [94]). As part of their work, they develop a number of tools with which to study the photometric variability of these stars, some of which we use and describe in what follows. More recent studies, such as Aigrain et al. [4], are taking advantage of present capabilities to study the impact of these photometric variations on RV measurements.

We endeavor to compare measured RV variations with the photometric variability observed by *Kepler*, whose precision has unveiled the low-level variability of a large number of stars. Section 4.2 describes our data and observations. Though small, our sample is uniquely important because it is currently the only overlap set between the highest precision light curves and the highest precision RV measurements.

Section 4.3 presents the results of our statistical comparison between the photometric and RV variability measures. We show that the RV jitter is not correlated with the overall amplitude of photometric variations, as might be expected if the RV jitter is driven by features such as spots, but is strongly correlated with the complexity of the photometric variations as measured by the number of significant components in the Fourier spectrum of the light curve. We compare this finding with the predictions of the simple spot model of Aigrain et al. [4] and the simple rotational model of Saar et al. [116]. We find that the simple spot-based model cannot reproduce the observed RV variations for our stars, underestimating the observed jitter by factors of 10–1000, except for the one star with the largest amplitude (presumably spot driven) photometric variations. The simple rotational model of Saar et al. [116] — which attempts to include the effects of plages — fares better, underpredicting the observed RV variations by factors of 1.5–10.

Finally, we place these results in the context of the new photometric evolutionary diagram introduced by Bastien et al. [20], showing that the stars with the largest RV jitter variations are those that have evolved onto the "flicker floor" sequence in that diagram, which appears to mark a transition in the photometric and RV variability characteristics of otherwise quiet stars prior to and during their evolution as subgiants. We assess and summarize our results in Section 4.4.

4.2 DATA

4.2.1 Description of Sample

The California Planet Search is a radial velocity planet search campaign that, using Keck Observatory in its investigations [136], has monitored some stars for 15 years [cf. 67]. A small fraction of their target stars lie in the *Kepler* field, enabling a comparison between their photometric variability characteristics, their levels of chromospheric activity and their RV scatter. Spectral types, RV RMS values and *Kepler* IDs, among others, are listed in Table 4.1. The chromospheric activity indices in the table are averages of the time-series measurements of Isaacson & Fischer [72]. All of the stars in the sample are inactive according to the definition of Baliunas et al. [12].

Our sample of 12 stars comprises primarily G and K stars. Based strictly on surface gravities measured spectroscopically or obtained from the *Kepler* Input Catalog [31], most of these stars are dwarfs. However, the true $\log g$ values of the stars as determined spectroscopically and through the analysis presented in this study indicate that the stars span a range of $\log g$ from 2.5 to 4.5, and thus include 7 main sequence dwarfs ($\log g \geq 4.1$), 3 subgiants ($3.5 < \log g < 4.1$), and 2 red giants ($\log g < 3.5$). The available spectroscopic $\log g$ for the sample are included in Table 4.1, as well as the $\log g$ determined from our analysis of the light curve "flicker" as described in Section 4.3.3.

Given that the stars were selected for the RV planet survey based on their low S index activity [48], we expect these chromospherically inactive stars to display low levels of photometric variability, and indeed the *Kepler* light curves bear this expectation out through their very low photometric amplitudes of less than 3 mmag (Table 4.1 and Fig. 4.1). Despite the very low photometric variability amplitudes for the entire sample, the stars exhibit a large range of RV variations; one star, a rapidly rotating F star, has an RV RMS of 135 m s^{-1} (see Table 4.1).

Table 4.1. Stellar Parameters and Variability Statistics

Star Name	Kepler ID	Range[a]	X_0[b]	NPP[c]	P_{rot}[d]	flag[e]	$v \sin i$[f]	S Index[g]	RV RMS			V_{mac}[k]	F_8[l]	$\log g$		B-V	T_{eff}
									Measured[h]	Aigrain[i]	Saar[j]			Spectroscopic[m]	KIC[n]		
HD 173701	8006161	3.06	5	3	32.9	A	1.83	0.214	5.7	3.72	3.2	4.6	4.36	4.53	3.634	0.843	5399
HD 176845	4242575	0.95	23	7	3.0	B	33.1	0.208	135.5	4.82	32.6	3.2	3.77		4.243	0.528	6252
HD 177153	6106415	0.09	45	13	42.8	C	4.25	0.154	5.0	0.02	1.3	3.6	4.34	4.20		0.569	5993
HD 179306	3430868	0.83	62	20	42.2	C	0.4	0.115	8.6	0.21	2.2	4.7	3.14		4.584	0.910	5297
HD 182756	5184732	0.92	4	1	20.5	A		0.147	3.4	0.56			4.22		4.313		
HD 183298	12258514	0.42	8	4	7.3	B	0.5	0.158	4.3	0.38	3.3	3.7	4.14		4.301	0.593	5922
HD 183473	7201012	1.71	6	2	60.3	B	2.5	0.170	7.2	0.84	1.6	4.1	3.84			0.728	5664
HD 185351	8566020	0.57	39	4	93.0	C	1.0	0.190	9.6	0.32	1.3	5.1	3.41	3.37		0.928	5067
HD 186306	7970740	0.26	6	1	36.9	A		0.177	2.7	0.12			4.51		4.414		
HD 186408	12069424	0.22	25	1	24.0	B	2.8	0.145	4.0	0.15	2.7	4.0	4.08	4.34		0.643	5781
HD 186427	12069449	0.10	21	3	31.5	B	2.2	0.148	3.0	0.05	2.2	4.1	4.34	4.35		0.661	5674
HIP 93703	8547390	1.48	33	18	52.2	B	1.8	0.116	13.6	0.78	2.7	5.3	2.55		4.609	1.127	4919

[a] In ppt, obtained from Basri et al. [18]

[b] Number of zero crossings derived from the light curve smoothed by 10 hour bins [18]

[c] Number of significant periodogram peaks [18]

[d] Photometric rotation period derived from the Quarter 1–4 *Kepler* light curves, in days

[e] Quality flag for rotation period. A: probable rotation period; B: questionable; C: improbable

[f] In km/s

[g] Obtained from Isaacson & Fischer [72] and Wright et al. [142]

[h] Measured, in m/s, with planets and long term trends removed

[i] In m/s, predicted from Aigrain et al. [4]

[j] In m/s, predicted from Saar et al. [116]

[k] Macroturbulent velocity, calculated according to Valenti & Fischer [134], in km/s

[l] Derived according to Bastien et al. [20]

[m] From Valenti & Fischer [134]; HD 185351 is unpublished

[n] From the Kepler Input Catalog [31]

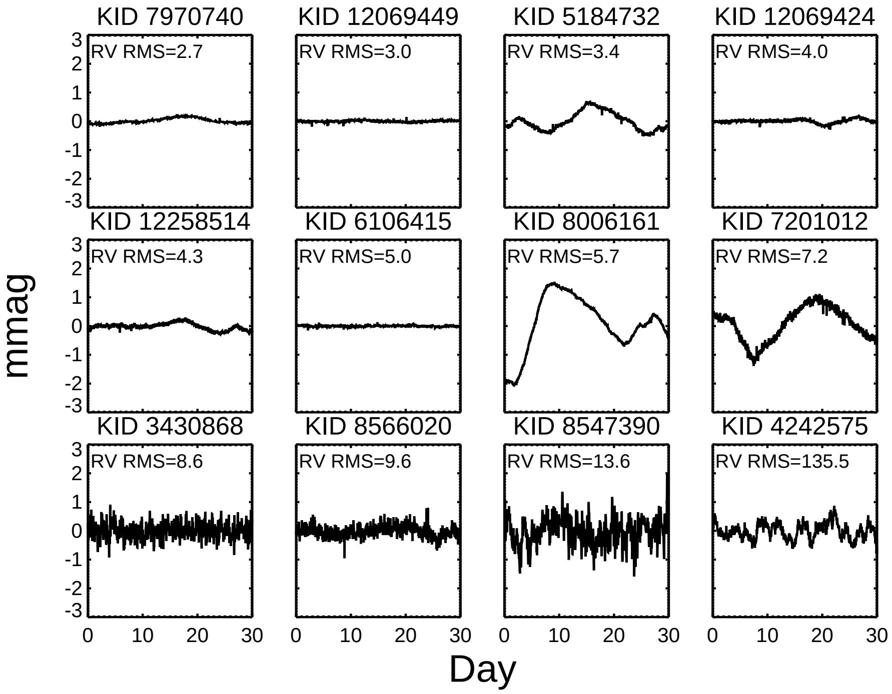

Figure 4.1: Quarter 1 *Kepler* light curves of the stars examined in this study, reduced as in Basri et al. [18] and sorted in order of increasing RV RMS. All are shown on the same scale, and the RV RMS in m s^{-1} is indicated for each star. The *Kepler* light curves reveal that stars with higher RV RMS tend to display higher frequency photometric variations. The title of each plot lists the star's *Kepler* ID. We derive rotation periods from Quarters 1-4 but here only show the Quarter 1 light curve to better highlight the high frequency content of each light curve.

4.2.2 Measurement of Radial Velocity Jitter

The radial velocity time-series measurements, shown in Fig. 4.2, were obtained in support of the California Planet Search program and made at the Keck and Lick Observatories (see also Isaacson & Fischer [72], Johnson et al. [73], and Wright [143]). For each star, we combined the velocities into 2 hour bins, weighting each velocity by the random ("internal") errors derived from the variance in the velocities reported from each section of the spectrum [33]. We then calculated the standard deviation of these binned observations' precise differential Doppler velocities. We note that resulting RV RMS values less than ~ 4 m s^{-1} may be dominated by instrumental systematics and shot noise. Such values reported herein are therefore upper limits. Finally, throughout the text we use the term 'RV jitter' to be synonymous with RV RMS. We emphasize that our use of these terms does not assume nor is intended to imply that the observed variations are simple Gaussian or 'white' noise; the photometric and RV variations we utilize in this work are in most cases substantially larger than the measurement errors and reflect real, if stochastic, variations of astrophysical origin.

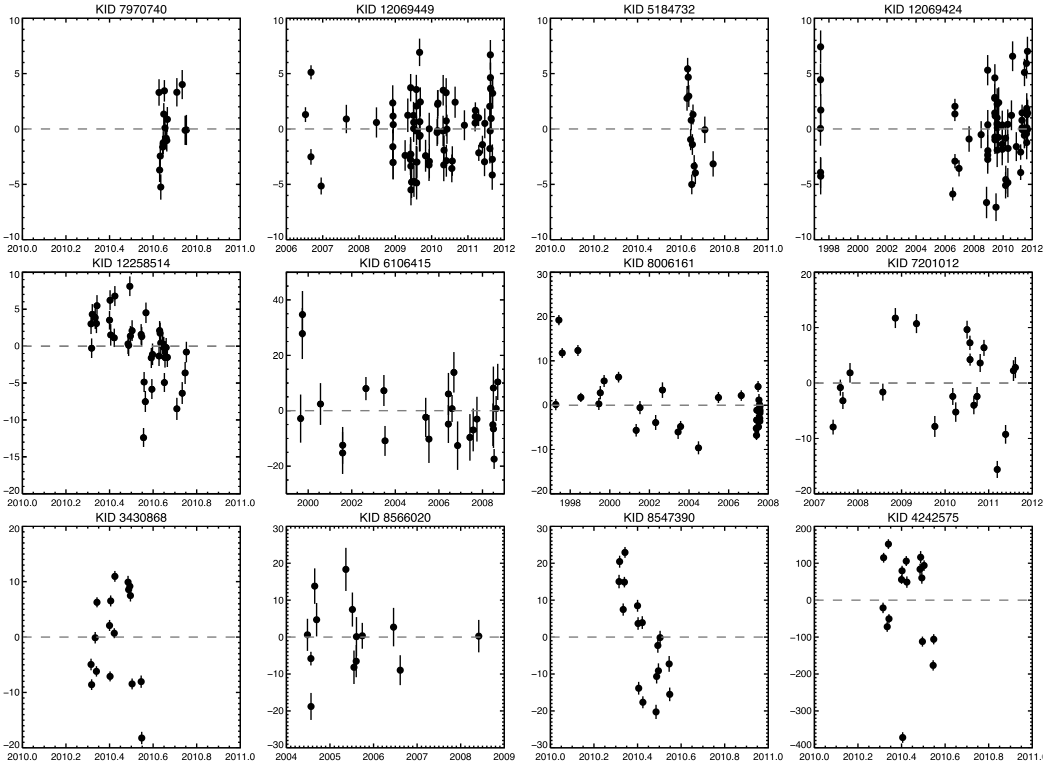

Figure 4.2: Radial velocity time-series of the stellar sample, with date on the x-axis. The y-axis is in m s^{-1}. Note the different axis scales for each panel. Each plot lists the *Kepler* ID in its title, and we show the stars in order of increasing RV RMS. Notes on individual stars are in Section 4.2.2.

4.2.2.1 Notes on Individual Stars

Kepler ID 4242575: This rapidly rotating star has the highest RV jitter in the sample, with an RMS of 135.5 m s^{-1}, measured across a span of 3 months. An outlying low point drives some of this; a robust RMS calculation yields a value of 119 m s^{-1}, but we adopt the former value for this work.

Kepler ID 6106415: We report 25 Lick velocities taken between 1999 and 2009. We reject 10 measurements taken between 1998 and 2000 which have internal measurement errors greater than 10 m s^{-1}. The median internal measurement error for this set of observations is 7.5 m s^{-1}. The RV RMS derived from these observations is 12.6 m s^{-1}, unexpectedly elevated given this star's very low photometric amplitude. Keck observations taken in 2013 yield an RMS of 5 m s^{-1}, suggesting that instrumental effects dominated the Lick measurements. We adopt the Keck RV RMS value in what follows.

Kepler ID 12069424: We find an RV RMS of 3.2 m s^{-1} after fitting and subtracting a strong linear trend due to the binary motion of 16 Cyg A about 16 Cyg B. In this work, we adopt an upper limit of 4 m s^{-1}. Given the internal errors, this choice of RV RMS does not make a significant difference.

Kepler ID 12069449: We report 75 measurements taken since November 2011 for this object after subtracting a best-fit one planet model to the known planetary companion.

Kepler ID 8547390: This star shows evidence of a linear trend in the velocities, but given the short span of the observations, this may simply be correlated astrophysical jitter. The RMS about the linear trend is 9 m s^{-1}.

4.2.3 Measurement of Rotation Periods

We derived the periods both by visually inspecting the light curves and by analyzing the Lomb-Scargle periodograms of those light curves [87, 120]. The Quarter 1–4 light curves folded on the derived periods, and the associated periodograms, are shown in Fig. 4.3 and 4.4. For most of the stars the periodogram reveals a clear, strong peak that we select as the likely rotation period. In some cases (for *Kepler* ID 8547390, for instance), we found a few strong contender periods (here, 52.2, 61.6 and 69.9 days) based on their power in the Lomb-Scargle periodogram. In such cases, the true rotation period is unclear. Additionally, discontinuous jumps in the reduced Quarter 3 light curve of *Kepler* ID 12069424, due to instrumental artifacts, obscure the true rotation period. We selected its probable rotation period based on analysis of Quarters 1, 2 and 4, together with inspection of subsequent *Kepler* Quarters, rather than relying on the strongest peak in the periodogram.

Whenever possible, we compared our rotation periods with $v \sin i$ measurements (Fig. 4.5), and we adopted radii from Cox [40]. In some cases the periodograms are complex and therefore our interpretation of the periodogram for the most likely rotation period is subjective. This complexity manifests in the folded light curves also (Fig. 4.3). The principal results of this paper do not depend strongly on the rotation periods adopted here. Still, the generally good correspondence between the photometrically derived rotation periods and the periods inferred from $v \sin i$ suggests that our newly derived photometric rotation periods are likely to be accurate. The rotation periods and $v \sin i$ measurements are in Table 4.1.

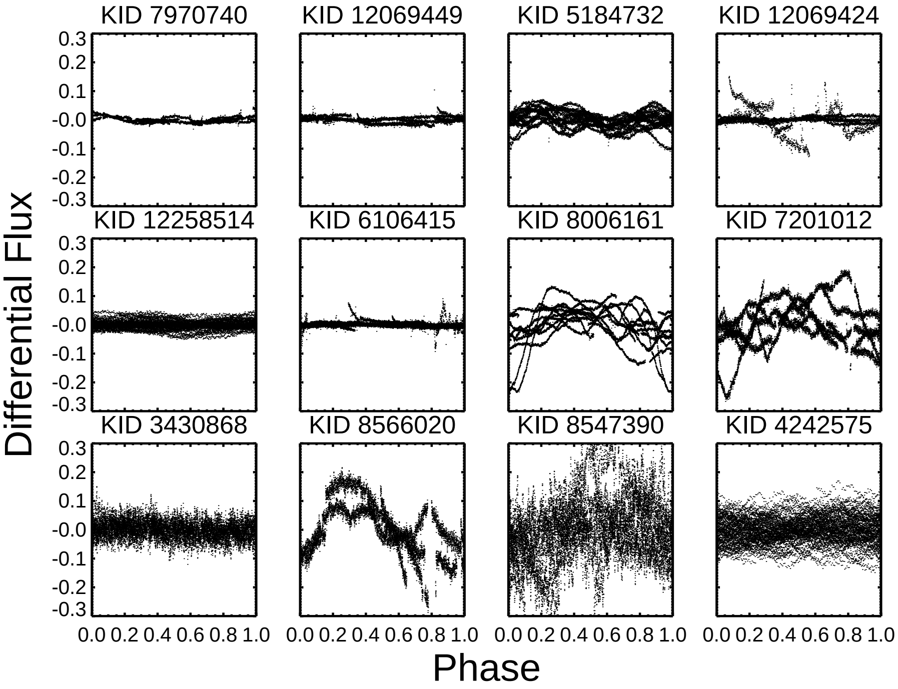

Figure 4.3: *Kepler* Quarter 1 through 4 light curves, reduced as described in Section 4.3.2 and folded on their derived rotation periods. The light curves show great complexity on these longer timescales due, among others, to the growth and decay of active regions. Plots are in order of increasing RV RMS.

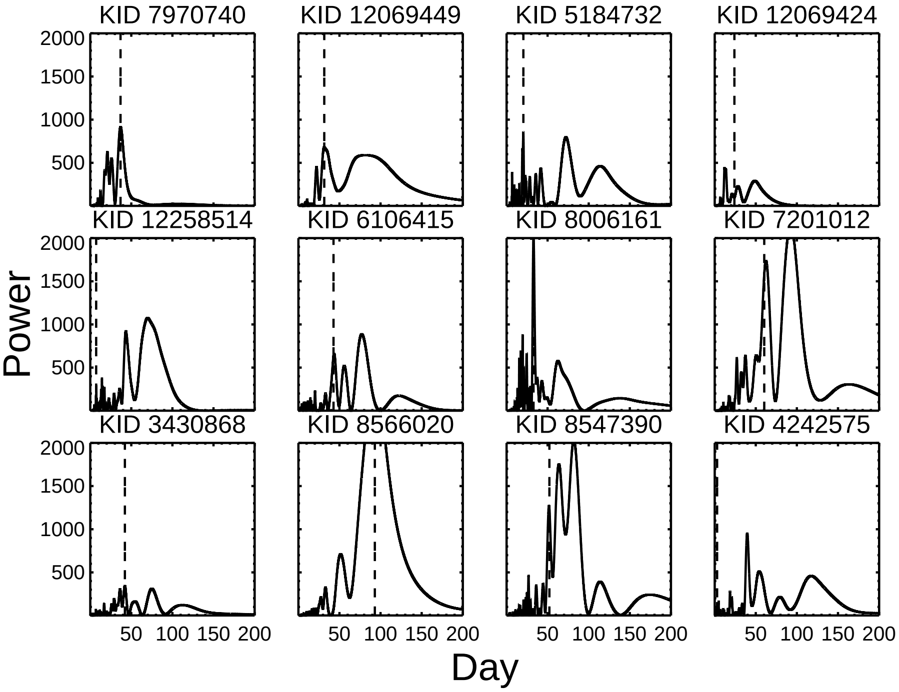

Figure 4.4: Lomb-Scargle periodograms of the Quarters 1 through 4 *Kepler* light curves, in order of increasing RV RMS. All plots are on the same scale. The dashed line demarks the stellar rotation period. The selection of the likely rotation period is subjective due to the complexity of the light curves and their corresponding periodograms. See text for notes on individual objects.

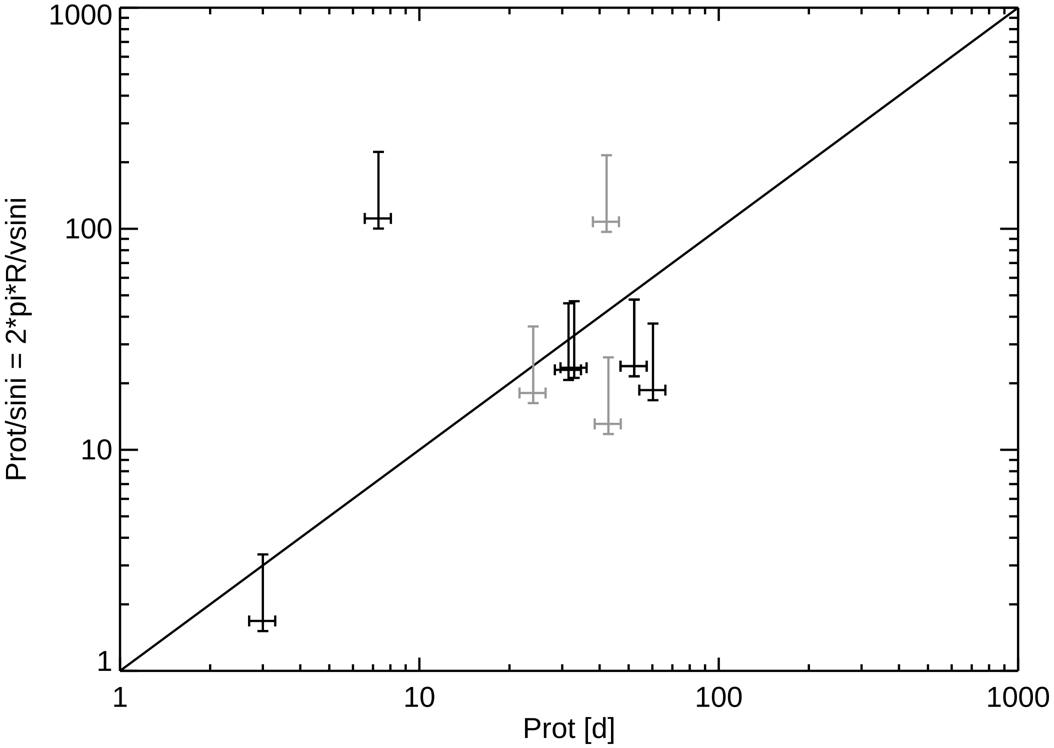

Figure 4.5: **Derived rotation periods compared with rotational velocity:** Where possible, we compared our photometrically measured rotation periods with rotational velocities: the complexity of the light curves, coupled with the low amplitudes of the photometric variations, could otherwise result in erroneously derived rotation periods in some cases. There nonetheless exist discrepancies, and we include quality flags on our rotation periods in Table 4.1. We represent in gray stars with a quality flag of C (signifying that the measured rotation period is unreliable). The solid line is a line of equality between the two plot axes. We estimate possible 10% errors on the light curve rotation periods, a factor of 2 error on the $v \sin i$ in the low direction (meaning that the actual $v \sin i$ could be half the measured value), and 10% error on the $v \sin i$ in the high direction (i.e., it is unlikely that the $v \sin i$ is much larger than that measured).

4.2.4 Photometric Variability Properties of the Sample

Basri et al. [18] used *Kepler* Quarter 1 data to broadly characterize the variability of all ∼150 000 stars being monitored. The observations took place between 13 May 2009 and 15 June 2009, a span of ∼33.5 days, and they restricted themselves to the Long Cadence data, whose cadence is 29.42 minutes, for their analysis. For each light curve, they determined the following variability metrics: the number of zero crossings in the light curve smoothed by 10 hour bins (a measure of the degree of short timescale complexity in the light curve); the variability range (a measure of the peak-to-peak amplitude of variability in the light curve); from the Lomb-Scargle periodograms of the light curve, the number of significant peaks (those whose strength is at least 10% that of the strongest one); and the four-point RMS, which measures the amount of high frequency variations present in the light curve (below we replace this with the sixteen-point RMS, which we refer to as the "8-hr flicker" or simply F_8).

Basri et al. [18] additionally categorized stars into three groups according to both amplitude of variability and maximal peak height in the Lomb-Scargle periodogram. In order from photometrically quiet to loud, the groups have photometric amplitudes of <2, 2–10, and >10 mmag, respectively. The quietest group in terms of the periodogram shows peaks whose heights are <30 in normalized power units. Based on this categorization, all of the stars considered in this work are photometrically very quiet, having variability amplitudes less than 3 mmag. This likely reflects the preference of the California Planet Search target selection for the quietest stars. But none of them meet the *peak periodogram height* requirements for the quiet category: the maximum periodogram heights range from ~ 38 to ~ 715. *In other words, the stars in this work are very low-amplitude variable stars that exhibit strong features in their Fourier power spectra, oftentimes multiple strong features.* Fig. 4.1 shows the light curves of the stars in this study.

4.3 RESULTS

The principal results of this study are presented as follows. First, we assess simple statistical correlations between RV and photometric variability measures in order to identify the primary photometric drivers of RV jitter. Next, we use two different models of photomteric and RV variations to examine the degree to which these models can reproduce the observed correlations for photometrically quiet stars such as comprise our sample. Finally, we place the observed photometric and RV variations in the context of the "flicker" evolutionary diagram newly presented by Bastien et al. [20].

4.3.1 Light Curve Periodogram Structure, Rather than Simple Photometric Variability, Encodes RV Jitter

We compare the measured RV RMS values with the variability statistics developed by Basri et al. [18] described in Section 4.2.4. To determine the significance of the correlations, we calculate a Kendall's τ statistic, a nonparametric rank-correlation test [108]. Given the presence of censored data (upper limits) in our set of RV measurements, which the canonical Kendall's τ test is not equipped to handle, we employ the procedure of Akritas & Siebert [7] implemented in the R statistical analysis soft-

Table 4.2. Statistical Confidence of Correlations for Measured RV RMS Values

Pair	Confidence[a]	Confidence incl. Outlier[b]	Sign of Correlation
RV RMS vs. Variability Range	80%	86%	positive
RV RMS vs. X_0	77%	74%	positive
RV RMS vs. Number of Periodogram Peaks	98%	98%	positive
RV RMS vs. Rotation Period	97%	76%	positive
RV RMS vs. F_8-based log(g)	97%	97%	negative

[a] Statistical confidence obtained from the Kendall's tau statistic, properly accounting for censored data [7].

[b] Confidence obtained from the Kendall's tau statistic when the star with the highest RV RMS is included in the sample.

ware package[1] (see also Helsel [61]) which correctly takes censored data into account. We list all correlation test results for the measured RV RMS versus photometric variability measures in Table 4.2.

The amplitude of photometric variability in dwarf stars is well-known to be correlated with the level of chromospheric activity, to the point that it is sometimes used as a proxy for activity when no such measurement is available (as, for instance, in Chaplin et al. [35] and Gilliland [56]). However, we find that RV jitter is not strongly correlated with the amplitude of photometric variability: a Kendall's τ test yields a confidence of 80% when we exclude the star with the highest RV RMS and 86% when we include it. Such a finding, while perhaps counterintuitive, is not surprising given that chromospheric activity and RV RMS are only weakly correlated even in dwarfs, as Saar et al. [116] demonstrate with a sample comprised of a range of spectral types. We thus confirm that amplitude of photometric variability by itself is a poor predictor of RV jitter.

---

[1] http://www.r-project.org

Nonetheless, we find that RV jitter is strongly manifested in photometric variability in other forms, namely in the structure of the photometric variability's Fourier power spectrum. We show a log-log plot of the RV RMS compared with the *number* of significant periodogram peaks (those at least 10% as strong as the maximum periodogram peak) in Fig. 4.6. This is a key result of this work, with a Kendall's τ confidence of 98% (see Table 4.2): low-amplitude variable stars that are noisier in RV have additional frequency components in the corresponding light curve.

This finding seems to indicate that there is only one dominant frequency of variability in the light curve of the low RV RMS stars while, as additional significant frequencies become manifest in the light curves, the RV RMS increases. The Lomb-Scargle periodogram may therefore be used to estimate the RV RMS of low-amplitude photometrically variable stars such as those examined in this work. We also note that this correlation holds for the range of evolutionary states examined here, with log(g) ranging from 2.5 to 4.5.

Figure 4.6 shows a variety of linear fits to the data. We fit simple linear regressions to samples including and excluding the outlier (black lines in the figure). We additionally fit, and take as more robust, regression lines using estimators that properly account for the censored data points in our sample: the slope is obtained from the Akritas-Theil-Sen estimator [6], and the intercept is a median residual from the Turnbull estimator [133, 61]. We present the following as a fit to low photometric amplitude variables with RV RMS $\lesssim 20$ m s^{-1}:

$$RVRMS = (3.8 \pm 1.7 \text{ m s}^{-1}) \times (N_{peaks})^{0.3 \pm 0.1} \tag{4.1}$$

where N_{peaks} is the number of significant Lomb-Scargle periodogram peaks, and the RV RMS is in m s^{-1}. For the uncertainties on the fit coefficients, we adopted the range of values from the three linear fits shown in Figure 4.6.

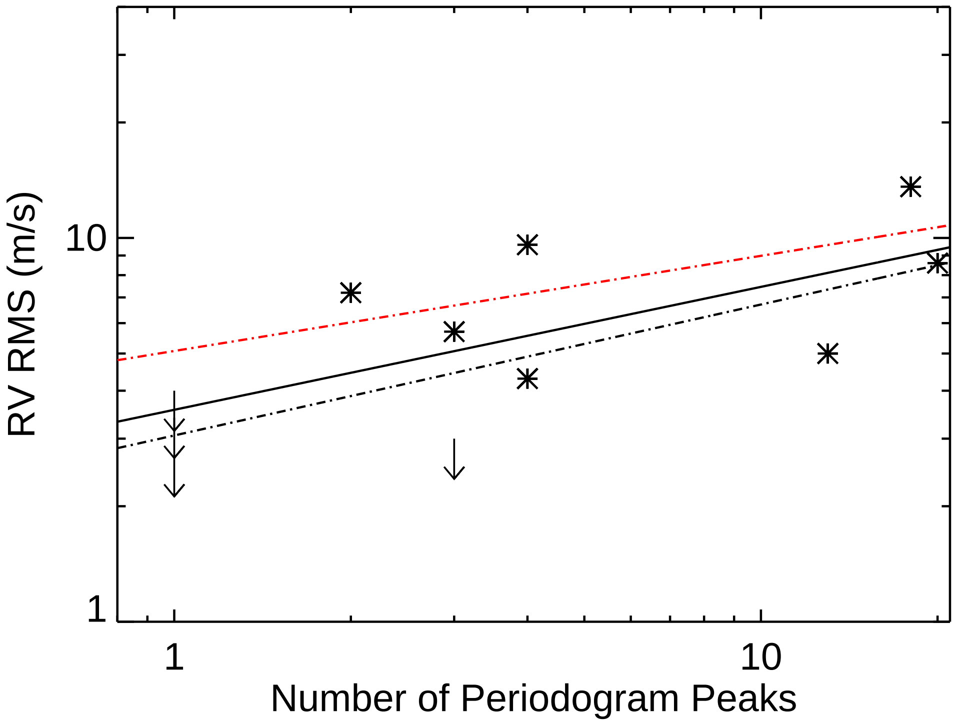

Figure 4.6: **The RV RMS of low-amplitude variable stars correlates with the number of significant periodogram peaks,** where "significant peaks" are those that are at least 10% as strong as the highest one. For stars with RV variations less than 20 m s^{-1} (i.e., excluding the one outlier with RV RMS=135.5 m s^{-1}), the RV RMS correlates with the number of frequency variations in the light curve, a finding that is statistically significant. An outlier, with an RV RMS of 135.5 m s^{-1}, lies outside the plot. The lines are linear fits to the data: black lines represent linear fits to stars with RV RMS less than 20 m s^{-1}. In red is a linear fit that includes all stars in the sample. Dot-dashed lines are more statistically robust fits to the data (see text). The variability statistics used here were measured from the *Kepler* Quarter 1 light curves as reported in Basri et al. [18].

The number of light curve zero crossings, though not highly statistically significant on its own (Table 4.2), seems to corroborate this result, providing here a measure of the high-frequency variability in the light curves. Indeed, the power spectra of those objects with large $N_{\rm peaks}$ tend to show many peaks at high frequencies. The light curves of stars with a small number of zero crossings exhibit longer timescale photometric variations while those light curves with many zero crossings tend to have lower amplitudes and display higher frequency light curve variability, evidenced by the stochasticity of their light curves in Fig. 4.1.

RV jitter is therefore evidently sensitive to higher frequency photometric variability in low amplitude variable stars. Indeed, this trend can even be detected by visual inspection of the light curves in Fig. 4.1. The light curves, sorted by increasing RV RMS, show a general progression in their qualitative behavior from relatively low frequency variations to increasingly stochastic variability. The latter stars, despite appearing "non-variable" by traditional standards of photometric variability amplitude, possess much more complex high-frequency variability, and in turn display the highest levels of RV jitter. Of course, the detailed behavior across Fig. 4.1 is not simply monotonic as some stars exhibit photometric variations with both low- and high-frequency content. Nonetheless it is the high-frequency variability that appears to be most important for driving the RV jitter. For example, comparing *Kepler* IDs 8006161 and 7201012 in Fig. 4.1, we see similar overall amplitudes of photometric variations and similar low-frequency content. However, the latter star also exhibits significant high-frequency variations superposed on the low-frequency variation, and this star exhibits a larger RV RMS. We revisit this diversity of light curve behavior and its impact on RV jitter in Section 4.3.3.

4.3.2 Spot Models Systematically Under-Predict RV Jitter in Photometrically Quiet Stars

As noted above, the stars in our sample all have photometric amplitudes below ∼3 mmag, a poorly explored regime of Sun-like stars. We have also seen in the previous section that these stars, despite being very photometrically quiet, do evince a strong correlation between the RV jitter and the complexity of their light curves, as measured by the number of peaks in the Fourier spectra of the light curves. Here we examine two models that have been previously developed to estimate RV jitter from light curve variations, in order to assess the ability of these models to reproduce the results presented above. We find that these models systematically underestimate the observed RV jitter.

4.3.2.1 Estimation of RV Jitter from Direct Light Curve Modelling with Spots

Aigrain et al. [4] provide a way to estimate RV variations due to activity from well-sampled light curves, assuming a simple spot model, which we apply to our sample. We processed the raw *Kepler* light curves to remove artifacts using a 3-point median filter with 3σ clipping. We then fit a straight line to the data, divided by it, and computed the auto-correlation function of the light curve. In order to identify the dominant timescale of the variability, we located the first peak where the auto-correlation function is zero, and we then smoothed the light curve on 1/10th of that timescale using an iterative nonlinear filter (see Aigrain & Irwin [3]). Finally, as in Aigrain et al. [4], we computed the time-derivative of the light curve and used it, along with the smoothed light curve, to simulate the RVs. We note that the resulting RVs should be taken with care given as the processing of the light curves does not always properly handle glitches and jumps in the data.

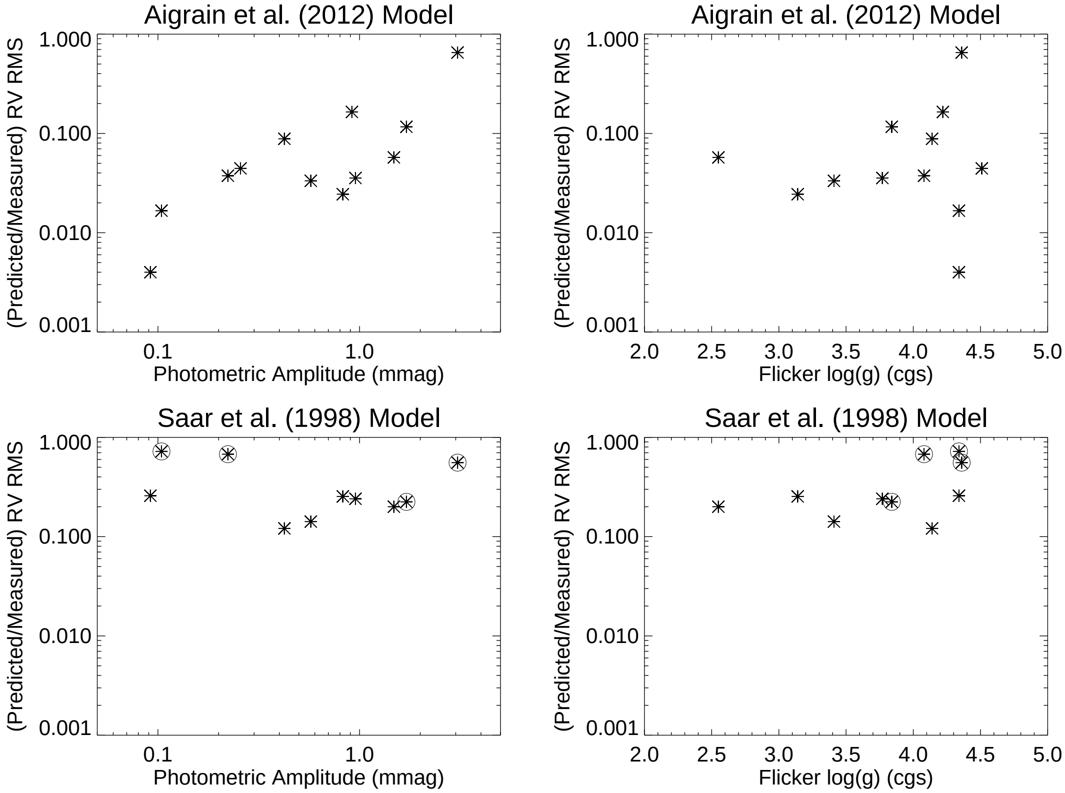

Figure 4.7: **Comparisons between measured and model-predicted RV RMS for photometrically quiet stars:** The *left* panels show how the agreement between the measured RV RMS and that predicted from two different spot models depends on the amplitude of photometric variations. The agreement in both cases generally improves as the photometric amplitude increases. The photometric amplitudes shown here have not been corrected for the *Kepler* magnitude. The text describes how the predicted RV RMS is derived. The circled points in the Saar et al. [116] plots are those with less than 3 significant light curve frequency components: the three stars which show the best agreement with model predictions have few significant Fourier components in their light curves. *Right:* similar to the above but compared against our F_8-based log$g$. There is significant spread in the agreement for log$g > 4$. We show all plots with the same y-axis scale.

Table 4.3. Statistical Confidence of Correlations for RV RMS Values Predicted from Light Curve[a]

Pair	Confidence[b]	Sign of Correlation
RV RMS vs. Variability Range	99.96%	positive
RV RMS vs. X_0	81%	negative
RV RMS vs. Number of Periodogram Peaks	17%	positive
RV RMS vs. Rotation Period	41%	negative
RV RMS vs. F_8-based log(g)	70%	negative

[a] Using the model of Aigrain et al. [4]. There is no apparent outlier in the RVs estimated from the light curve (see Table 4.2).

[b] Confidence obtained from the Kendall's tau statistic.

We predicted the RV RMS with this model using the entire Quarter 1 light curve. Figure 4.7 shows the predicted versus observed RV RMS. The predicted RV RMS is systematically too small, by factors of 10–1000 times.

Table 4.3 lists the results of comparing the amplitudes of these simulated RVs with the various variability statistics used in this work. We find that the predicted RV RMS predicts a significant correlation only with the photometric range. This is in strong contrast with the measured RV RMS (Table 4.2), which is in fact far more sensitive to higher frequency variations than to overall range alone. The model used to simulate the RVs does not take such photometric variability into account, and it therefore does not reproduce the trends we find with the measured RV RMS.

We find (see Fig. 4.7) that the agreement between the measured and the simulated RVs improves when the photometric range reaches above a threshold of ~2 mmag, in effect when the photometric variations become more simply spot dominated. We note that the predicted RV RMS of the rapid rotator, otherwise an outlier in this work, also has a predicted RV RMS that is significantly discrepant with its measured

RV RMS. Its photometric amplitude is less than 1 mmag (Table 4.1), highlighting the relative importance of the amplitude of photometric variability over other factors in determining the success of such spot based models.

The true RV measurements were not taken continuously with the high and regular cadences of the *Kepler* data (which in turn become the cadences of the predicted RV light curves). Thus, in order to more realistically predict the RV RMS from the light curve, we also randomly sampled points from the calculated RV time-series, taking the same number of data points as that used to obtain the *measured* RV time-series and then calculating the predicted RV RMS. We performed 10^6 realizations and then took the mean and median of the resulting distributions. The overall conclusions are the same as those described above. Finally, we repeated the simulated RV RMS determination using *Kepler* Quarters 1–4, but the results do not significantly differ from those obtained using the Quarter 1 light curves alone. We thus opted to report the results for Quarter 1 to maintain consistency with the light curve variability statistics published by Basri et al. [18], which also used only Quarter 1 data.

It may be possible to improve the performance of this model in this regime. For example, if our hypothesis is correct that the RV RMS is linked to short-timescale photometric variability, then using a shorter smoothing length in the simulated RV jitter might give a better match to the measured RV jitter.

4.3.2.2 Estimation of RV Jitter from a Simple Rotational Model

We also estimate the RV jitter of the stars in our sample using the simple model presented by Saar et al. [116]. It is composed of two terms: a spot term and a convective term, with the latter also taking into account contributions from plage. We use as inputs into this model the B-V colors, $v \sin i$, macroturbulent velocities and effective temperatures listed in Table 4.1. The model is also strongly rotation period dependent, and we as such we utilize the rotation periods for our sample stars as measured in Sec. 4.2.3. We apply the model to our sample under the assumption that it largely contains dwarfs, as suggested by broadband photometric measurements (Table 4.1).

As shown in Table 4.1 and Fig. 4.7, this model also systematically underestimates the actual jitter, though only by 1.5–10 times. The agreement is better for some of the stars with gravities placing them firmly on the main sequence, as might be expected, but there are still a few instances of significant disagreement (Fig. 4.7). The number of significant photometric variability components is a key factor in determining the success of the model: dwarfs with a smaller number of periodogram peaks tend to show better agreement with the model. In Fig. 4.7, we highlight stars with up to three dominant Fourier components in their light curves: the three stars with Saar et al. [116]-predicted values that best match observations are those with few significant Fourier components in their light curves. Thus, limiting application of the model to true dwarfs does improve its ability to predict the RV jitter, but this by itself does not guarantee its success. The degree of complexity in the light curve remains a crucial factor.

We note that the convective term dominates the jitter estimate for these chromospherically inactive stars, and its contribution to the RV jitter may therefore be underestimated. One potential way to improve the convective contribution to the RV jitter is to scale this term according to the number of light curve frequency components.

4.3.3 RV Jitter Correlates with Position in the Photometric Variability Evolutionary Diagram of Bastien et al. [20]

Bastien et al. [20] have recently presented a new "photometric variability evolutionary diagram" based on analysis of a large sample of *Kepler* stars. This diagram captures the time evolution of stars from the main sequence to giant branch purely in terms of three measures of photometric variability: Range ($R_{\rm var}$, a measure of overall photometric variability amplitude), "flicker" (F_8, a measure of photometric variations on timescales of <8 hr), and the number of light curve zero crossings (X_0, a measure of the light curve complexity, similar to the number of dominant Fourier components in the light curve discussed above).

Here we briefly summarize the salient features of this diagram from Bastien et al. [20]. First, F_8 was shown to be a strong correlate of the stellar surface gravity, predicting $\log g$ with an accuracy of $\lesssim$0.1 dex, and thus serves as a tracer of the physical evolutionary state of a star. Stars' F_8 values increase systematically with decreasing $\log g$. Second, the diagram includes two main populations of stars. One group consists of main sequence dwarfs with small F_8 (consistent with their high $\log g$) but with a large spread of $R_{\rm var}$, representing the spin-down evolution of main-sequence dwarfs from rapidly rotating active stars to slowly rotating inactive stars. Another group of stars defines a remarkably tight sequence that Bastien et al. [20] referred to as the "flicker floor" sequence. This sequence comprises stars with a range of $\log g$, from dwarfs to red giants, whose F_8 increase as the stars evolve. Stars on the "flicker floor" sequence tend to be very slow rotators, have extremely low $R_{\rm var}$ (they sit on the "floor" of minimum possible $R_{\rm var}$), and have as a common feature a high degree of light curve complexity as indicated by a large X_0.

In Fig. 4.8 we show our study sample in the Bastien et al. [20] photometric variability evolutionary diagram ($R_{\rm var}$ vs. F_8, with symbol size proportional to X_0). Here, the RV RMS is represented by symbol color. Arrows depict the paths that stars follow in the diagram as they evolve from rapidly rotating, active main sequence stars at upper left, downward as they spin down and become less active, and finally along the "flicker floor" sequence as they evolve as subgiants toward the red giant phase.

It is clear from Fig. 4.8 that the stars with the largest RV RMS are those that have alighted onto the flicker floor sequence. In most cases, these are stars that have already begun their post-main-sequence evolution as subgiants, and thus their enhanced RV jitter may be attributed to their evolved status. The correlation between RV jitter and F_8 is also shown directly in Fig. 4.9; a Kendall's τ test gives a correlation with 97% confidence.

Thus, we find that the RV jitter of our sample stars can be explained by their placement in the photometric variability evolutionary diagram of Bastien et al. [20]. In large part for our sample, which includes several modestly evolved subgiants, the RV RMS can be predicted simply from the stars' F_8 (or equivalently their $\log g$; Fig. 4.9). Interestingly, there is a hint that the stellar evolutionary state is not the whole story. In particular, one dwarf (*Kepler* ID 6106415) has somewhat higher RV jitter than most other dwarfs of low photometric amplitude. What distinguishes

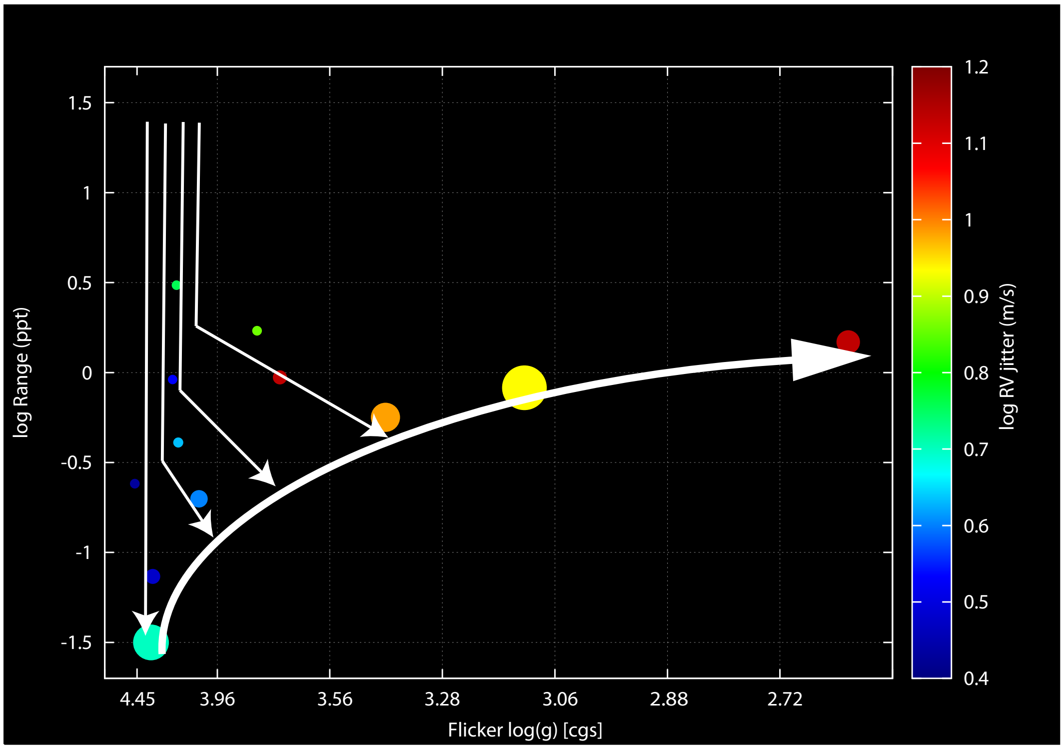

Figure 4.8: **Study sample shown in the photometric variability evolutionary diagram of Bastien et al.** [20]. Points are color-coded according to RV RMS, with the redder colors corresponding to larger RV RMS. The arrows depict how stars evolve in this diagram (see text). Dwarf stars are clustered to the left; those with comparatively large range show low levels of RV jitter. Stars lying on the "flicker floor" tend to exhibit large levels of RV jitter. In particular, more evolved stars show the expected higher levels of RV jitter; most of them lie on the "flicker floor."

this particular stars is its position on the F_8 floor, and hence its relatively large X_0. More generally, the stars with the highest RV RMS, ranging from unevolved dwarfs to evolved subgiants, are those that sit on the "flicker floor" sequence in the diagram. These stars' position on the flicker floor sequence also explains the very strong correlation between RV RMS and number of light-curve Fourier components (Sec. 4.3.1) as a manifestation of these stars' complex light curves (high X_0) despite their generally very low R_{var}.

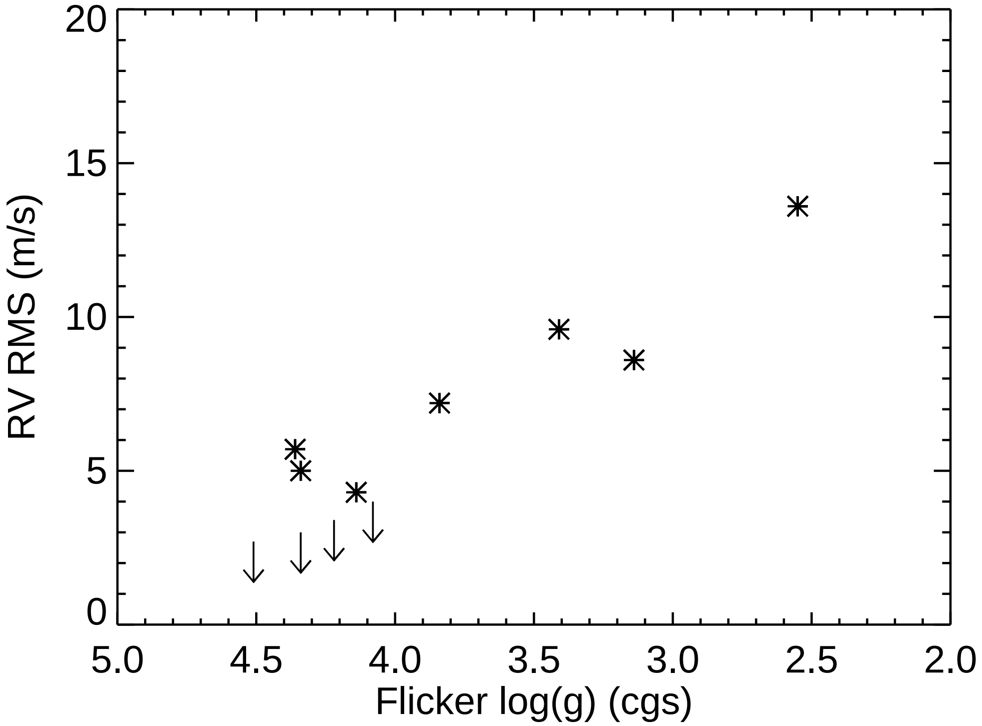

Figure 4.9: **Correlation between RV RMS and F_8-based log$g$:** RV RMS shows a strong anti-correlation with F_8-based surface gravity, with a confidence of 97%. A similar trend was found by Wright [143]. F_8 ("flicker") measures granulation power [20], indicating that the RV jitter of inactive stars is driven by convective motions on the stellar surface whose strength increases as stars evolve.

4.4 DISCUSSION AND CONCLUSIONS

In general, we find that RV RMS is quite sensitive to high-frequency light curve variations as well as to the number of significant frequencies that make up the light curve, apparently irrespective of spectral type for F, G and K stars. We find that one can use the number of significant peaks in the Lomb-Scargle periodogram to predict the RV RMS of variable stars whose amplitude of photometric variability is less than ∼3 mmag; we provide a simple power law relation in section 4.3.1. This also manifests in the number of light curve zero crossings, a crude measure of the Fourier complexity of the light curve. More generally, we have found compelling evidence that the stars with the largest RV jitter are those that have alighted onto the “flicker floor” sequence in the photometric variability evolutionary diagram of Bastien et al. [20], possessing low R_{var} but large X_0.

The object exhibiting the highest RV RMS is the principal outlier throughout this work. Though difficult to draw firm conclusions with one data point, we suggest that there may be different regimes of applicability of photometric variability-RV jitter relations; the relationship between photometric variations, particularly the number of Fourier components, and RV RMS perhaps changes for stars with RV RMS values exceeding $\sim$20 m s^{-1}. For such stars, the rapid rotation, and associated high level of chromospheric activity, may suppress the high frequency photometric variations that seem prevalent in the other stars in our sample [53, 35, 70].

Our findings, though comprised of several modest correlations, are based on the only sample of stars currently available with both light curves and RV measurements of exquisite precision, permitting us to probe a regime of activity and variability not possible heretofore. Indeed, we note that these stars are considered inactive by most standards; see, e.g., Baliunas et al. [12]. Our findings seem to paint the following picture: the light curve variations of the more chromospherically active stars are typically larger, presumably dominated by the rotational modulation of simple spot regions. Such stars tend to have fewer dominant peaks in their Fourier spectra, and these peaks tend to be at lower frequencies; they exhibit low levels of RV jitter. The opposite is true for the slowly rotating, less chromospherically active stars: they reside on the flicker floor sequence of the Bastien et al. [20] photometric variability evolutionary diagram, and the Fourier spectra of their light curves reveal many high frequency variations (their light curves show large X_0), which seem to drive their high RV variability. This picture only seems to hold, however, for a limited range of RV RMS values: the applicability of RV RMS-photometric variability- chromospheric activity relations may depend on factors such as type of photometric variability (here we dealt with low-amplitude variables $\lesssim$3 mmag), the particular range of RV RMS, and a narrow range of low-activity stars.

Previous work [e.g. 111] suggests that solar type stars may undergo a transition from spot dominated activity at high activity levels to faculae-dominated activity at low activity levels, and that this transition occurs at photometric variability levels of a few mmag. Thus our findings may suggest that the faculae dominated variability at slow stellar rotation and low chromospheric activity levels produces both lower amplitude photometric variations and higher RV jitter. This interpretation would also explain the failure of spot-based models to predict the RV jitter of these faculae dominated stars.

Applying the recently developed models of Aigrain et al. [4] to the *Kepler* light curves of our sample stars further corroborates the above scenario. These models, which are based on using coherent spotted stellar surfaces to model the photometric variations, accurately predict the RV jitter for the stars in our sample with simple, single-component photometric variations, but systematically underpredict the RV jitter for stars with multi-component, high-frequency photometric variations.

Our results hold primarily for stars with RV RMS values below ~20 m s^{-1}. In this regime, it seems that, using the measures examined in this work, stars with few significant Fourier components (or low X_0, situated well above the flicker floor sequence in the photometric variability evolutionary diagram of Bastien et al. [20]) are better targets for RV planet searches despite their larger amplitude photometric variations and larger chromospheric S indices. Conversely, those objects with larger RV variations, while manifesting more complex light curve variations, do nonetheless in general exhibit lower amplitude light curve variability, and thus could still serve as good candidates for low-amplitude transit signals.

CHAPTER 5

LARGER PLANET RADII INFERRED FROM STELLAR BRIGHTNESS VARIATIONS

Most extrasolar planets have been detected by their influence on their parent star, either gravitationally (the Doppler method) or by the small dip in brightness as the planet blocks a portion of the star (the transit method), and the mass (obtained via the Doppler method) or the radius (inferred from the transit method) is a function of the known mass or radius of the star, respectively. Therefore, the accuracy with which we know the masses and radii of extrasolar planets detected by these methods depends directly on how well we know those of the stars, usually determined from the measured stellar surface gravity, g. Recent work has demonstrated that the short-timescale brightness variations of stars can be used to measure g with an accuracy of 25 per cent or better [20]. Here, we use the measured short-timescale brightness variations for a large number of candidate planet-hosting stars to perform a re-assessment of the stellar parameters and determine the resulting impact on derived planet properties. The stars are found to be significantly more evolved than previously believed, having on average 40 per cent larger radii than previous estimates, with the result that many of the planets about these stars are ~40 per cent larger than measurements based on broad-band photometry had suggested.

NASA's Kepler Mission [25], which monitored the brightnesses of over 150,000 stars, has uncovered over 3,000 transiting planetary candidates [23]. In order to measure the temperatures and g of this large number of stars, the mission has of necessity relied on broad-band photometry, the most efficient method, but with uncertainties in g of 90 to 150 per cent [31]. Such uncertainties in g translate into similarly large uncertainties in the derived planet radii. Using 8-hr 'flicker' (alternatively, F_8) [20], which measures g from its correlation with granulation power in the light curves [91, 82, 42], we refine the stellar g for active Kepler Objects of Interest (KOIs, which include planetary candidates as well as confirmed planets) with magnitudes of KepMag < 13. We obtained from the NASA Exoplanet Archive (NEA) Cumulative Catalog (accessed on August 6, 2013; Akeson et al. [5]) the planet orbital properties, planet-to-star radius ratios, and the stellar temperatures, metallicities, and g values previously determined from broadband photometry/spectroscopy [31, 105].

With the Filtergraph data visualization tool [32], we represent the light curves of these 266 planet host stars on a photometric variability evolutionary diagram (Bastien et al. [20]; Fig. 5.1). This diagram traces the evolution of Sun-like stars with three simple measures of their brightness variations [18]: range (R_{var}), number of zero crossings (X_0), and root mean square on timescales shorter than 8 hours (F_8). Because the planetary transits can artificially boost the measured F_8, thereby resulting in an erroneously low g, we remove in-transit data points using the publicly available planet orbital parameters prior to measuring F_8. We find that most of the planet candidates orbit stars with R_{var} less than 1 ppt, reflecting the preference for searches around magnetically quiet stars, and F_8-based g greater than 3.5 (indicating they are dwarfs or subgiants). Some of the stars lie on the "flicker floor" and have surface gravities as low as 2.5, making them evolved giants. Comparing the g previously estimated from broadband photometry/spectroscopy versus the g newly measured via F_8 shows the latter to be systematically lower (i.e., less dwarf-like and more subgiant-like).

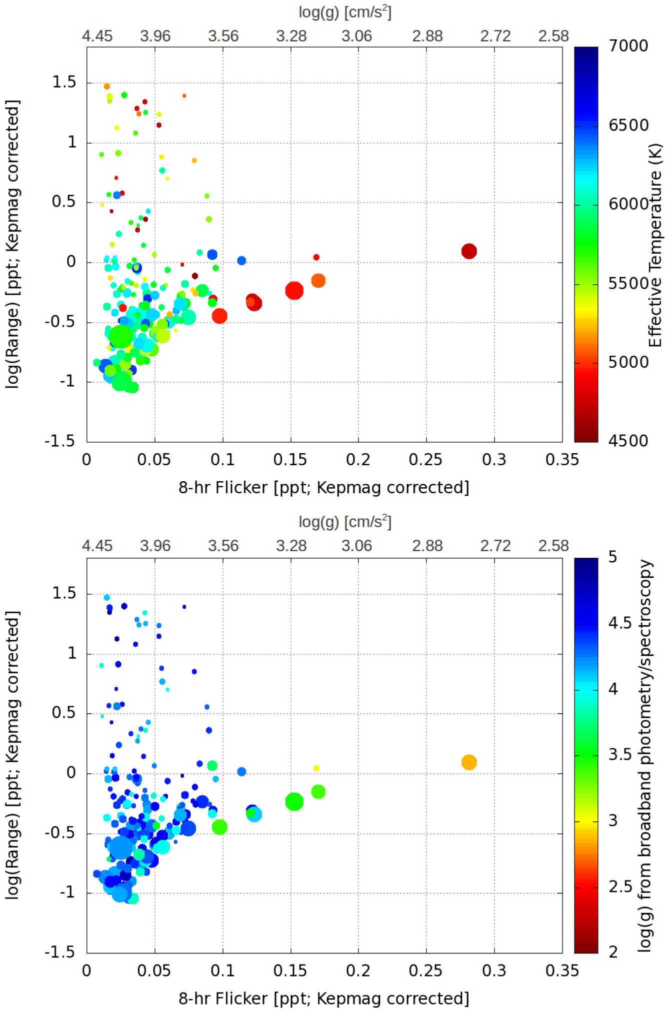

Figure 5.1: A snapshot of the distribution of evolutionary states of planet candidate host stars. Using three distinct measures of photometric variability [18], we show the evolutionary states of KOIs with Kepler magnitudes (Kepmag) brighter than 13. On the abscissa is 8-h flicker (F_8), which measures brightness variations on timescales of 8 h or less and is a strong tracer of g [20]. We show the F_8-based g scale at the top. We represent the amplitude of the photometric variations, R_{var}, on the ordinate, and the number of zero crossings (X_0) as the point size. Both R_{var} and F_8 are corrected for their magnitude dependence. *Top:* This diagram, color-coded by effective temperature [105], shows that a large fraction of Kepler planet candidates with F_8 less than 0.05 ppt (i.e., dwarfs) have R_{var}, a measure of surface magnetic activity, less than 1 ppt, partially reflecting the preference for targeting magnetically quiet stars. *Bottom:* Color-coded by g determined largely from broadband photometry [5], the diagram shows that broadband photometric measurements preferentially indicate that these stars are dwarfs, while F_8-based g suggests many of them are significantly more evolved, including a significant population of subgiants and red giants.

These KOIs have been used to reveal the distribution of exoplanetary radii [23], after correction for observational and selection biases [68, 104]. To examine the effect of the improved accuracy of the host star parameters based on our F_8-derived g, we have recalculated the radius-period distribution of the 266 KOIs described above (Fig. 5.2). The planet radii are determined from the NEA-reported planet-to-star radius ratios, and for the stellar radii we use the empirical relationship between stellar radius, effective temperature, g, and metallicity [132]. We use the metallicities and effective temperatures provided in the NEA together with our new F_8-based values of g.

The key impact of including F_8-derived g information is to significantly increase the median radius of the KOIs in the sample. We find that the median KOI radius is larger by 40 per cent compared to that inferred using the g reported in the NEA, though a number of objects show a more modest change in radius (Fig. 5.2c). This result stems directly from the new F_8-based g values being systematically lower than those previously reported, implying that many of the planet host stars are significantly more evolved than had been indicated by broad-band photometry/spectroscopy. In particular, 50 per cent of the planet-hosting stars have F_8-based g values indicative of modestly evolved subgiants and giants, whereas the g values that had been previously estimated largely from broadband photometry indicated that only 17 per cent were evolved stars. We also find fewer 1–1.5 Earth-radius planets than previous work has suggested.

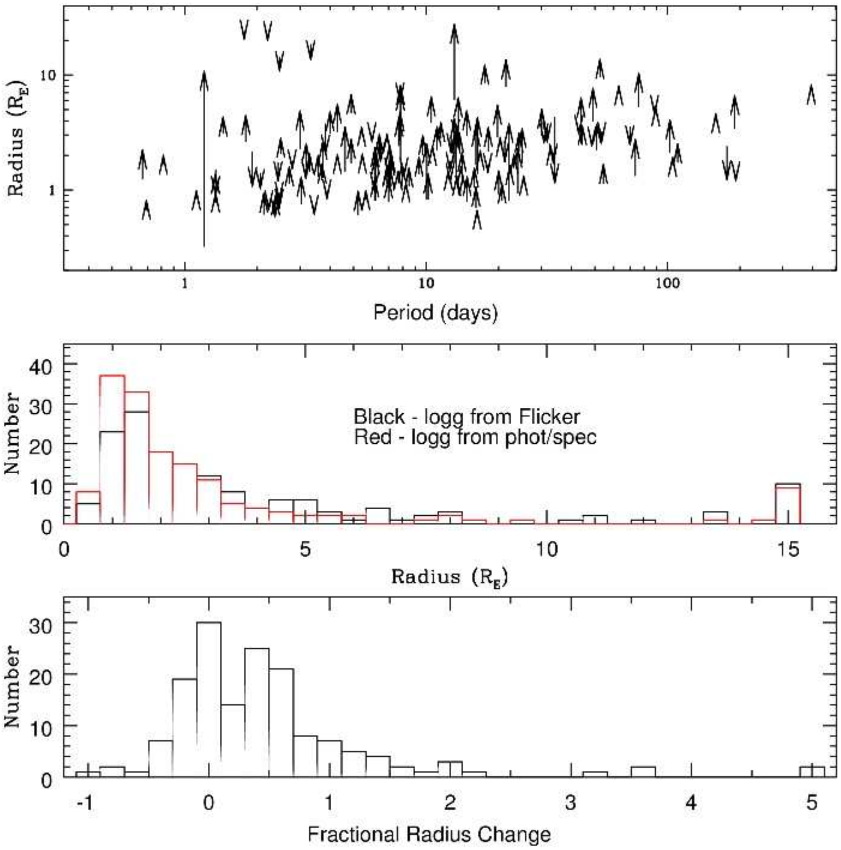

Figure 5.2: The distribution of planet candidate radii, according to stellar gravities from light-curve flicker. Top: With the exoplanet transit information, together with estimates of the stellar properties, we show the distribution of the planet orbital period against the exoplanet radius for KOIs brighter than Kepmag of 13. The arrows depict how planet radii shift in this diagram when they have g derived from F_8 (arrow head) vs. g estimated from broad-band photometry/spectroscopy (arrow tail). We derive stellar radii through empirical relations that yield this quantity given knowledge of the stellar g, effective temperature and metallicity [132]. Middle: The distribution of exoplanetary radii with stellar g obtained from F_8 (black curve) and broad-band photometry/spectroscopy (red curve). Using g derived from F_8 results in far fewer 1-1.5 Earth-radius planets than the other methods. Bottom: Fractional change in planet radius between F_8-based g and photometry/spectroscopy-based g. Using F_8-based stellar g results in a median exoplanet radius that is 40 per cent larger than suggested by broadband photometry-based g.

To compare our results with those expected based on the underlying stellar population, given the magnitude-limited nature of the Kepler sample, we simulated the Kepler field using the TRILEGAL Galactic population synthesis model [58]. The H-R diagram of the simulated population is shown in Figure 5.4a. For comparison, we show the H-R diagram of the actual sample, using F_8-based gs, in Figure 5.4b. The distribution of gs from our analysis compares very well with that expected from the simulated population, whereas the previously determined g show a distribution much more highly skewed toward larger, more dwarf-like values of g (Figure 5.3 and 5.4c). A two-sided K-S test gives a probability of 0.0001 per cent that the previously adopted g and the g from the simulated stellar population are drawn from the same parent sample, suggesting that the two are not drawn from the same parent sample, whereas a K-S test gives a probability of 56 per cent that the stars with F_8-based g are drawn from the same parent sample as the simulated ones. Evidently, for a magnitude-limited sample such as that considered here, modestly evolved subgiants represent a large fraction of the population. Methods that apply a strong prior favoring main-sequence dwarf g will systematically overestimate g for such a sample, and in turn systematically underestimate the planet radii.

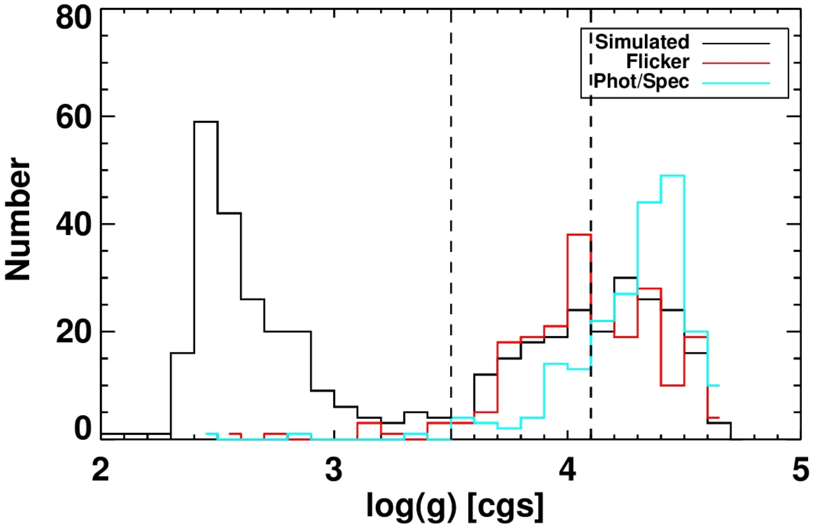

Figure 5.3: Stars with F_8-based stellar gravity trace the expected underlying stellar population. Distributions of simulated (black histogram) and planet candidate host stars with F_8-based g (red histogram) and broadband photometry/spectroscopy-based g (cyan histogram). The simulated distribution is from the TRILEGAL Galactic population synthesis model [58], in the direction of the Kepler field and using default model parameters, and limited to Kepmag < 13. As the Kepler mission sought to primarily target dwarfs, the distributions of KOI host stars are dominated by high g stars; the very large population of red giants with $\log g < 3$ seen in the simulated sample (black) is conspicuously missing in the actual planet host-star sample (red and cyan). For $\log g > 3$, we find good agreement between the simulated and the F_8-based g distributions: a two-sided K-S test gives a probability of 56 per cent that they are drawn from the same parent sample. The simulated distribution predicts that 45 per cent of the stars will be evolved subgiants ($3.5 < \log g < 4.1$; vertical lines), and the F_8-derived distribution suggests that 50 per cent of the stars are evolved. Stars with g derived largely from broadband photometry are biased towards higher g values and do not agree with the expected distribution: the two-sided K-S test yields a probability of only 0.0001 per cent that they and the simulated distribution are drawn from the same parent sample.

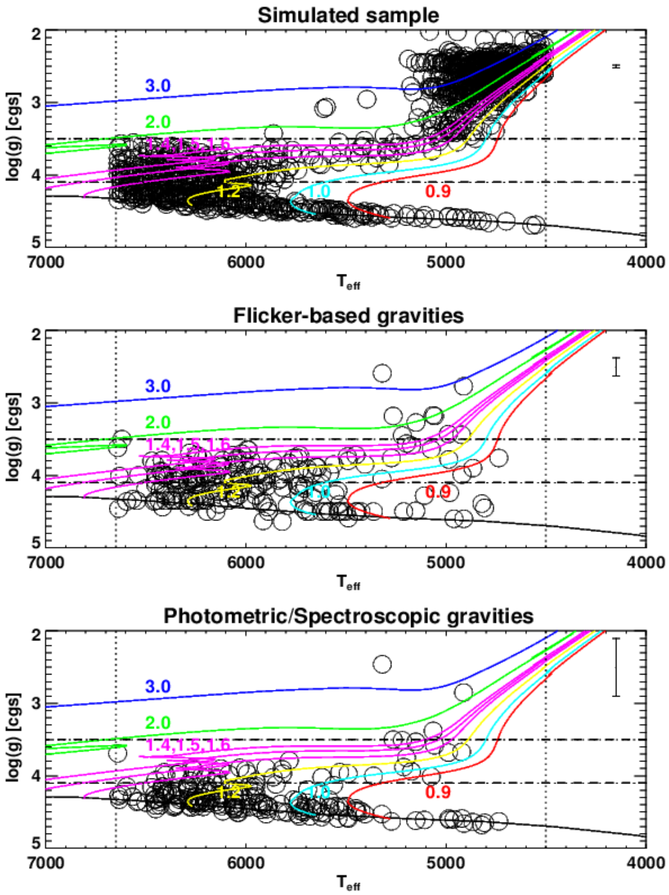

Simulated sample

Flicker-based gravities

Photometric/Spectroscopic gravities

Figure 5.4: H-R Diagram Distribution of Confirmed Planet and Planet Candidate Host Stars. We place the KOI host stars with g derived from F_8 (middle) and broadband photometry or spectroscopy (bottom) on an H-R diagram. The top panel shows the expected distribution of stars brighter than Kepmag of 13 on this same diagram. Colored curves represent the theoretical evolutionary tracks of stars of different masses (labeled in solar masses). Vertical lines demarcate the range of stellar effective temperatures that we consider in this study, 6650 K $>$ T$_{eff}$ $>$ 4500 K, for which the F_8-based g is calibrated [20]. The horizontal lines demarcate the range of g that we take to be modestly evolved subgiants ($3.5 < \log g < 4.1$). A representative error bar on g for each stellar sample is in the upper right of each panel. For the simulated sample (top), we show the typical error on g from asteroseismic analyses [36]. For the predominantly broadband photometry based g (bottom), we show the typical error on g [31]. For the F_8-based g (middle), the error bar is determined from the empirical relationship between g error and R$_{var}$ determined via comparison with the asteroseismic g [36] that we use for calibration of the F_8-g relation (Fig. 5.5). Ignoring the highly evolved red giants ($\log g < 3$) present in the simulated sample (top) but which are removed from transiting exoplanet studies by the Kepler mission, we find that the F_8-based sample (middle) traces the expected underlying stellar population (top) very well. By comparison, many objects with g previously estimated largely from broadband photometry (bottom panel) are strongly displaced towards main-sequence dwarf-like high g.

This finding, that the Kepler planet-hosting stars comprise a significantly more evolved population than originally assumed, has been suggested by spectroscopic and asteroseismic analyses of other samples of Kepler stars [135, 88, 50, 52, 71]. Detailed studies of individual planetary systems using asteroseismic g or g derived from high-resolution spectroscopy [27, 57, 49, 22, 14, 69] are expected to be more reliable. As we have shown here, F_8-based g may provide a significant improvement over broadband photometric g for ensemble analysis of global samples of exoplanets, and one cannot ignore the magnitude-limited nature of the stellar samples when inferring their ensemble properties.

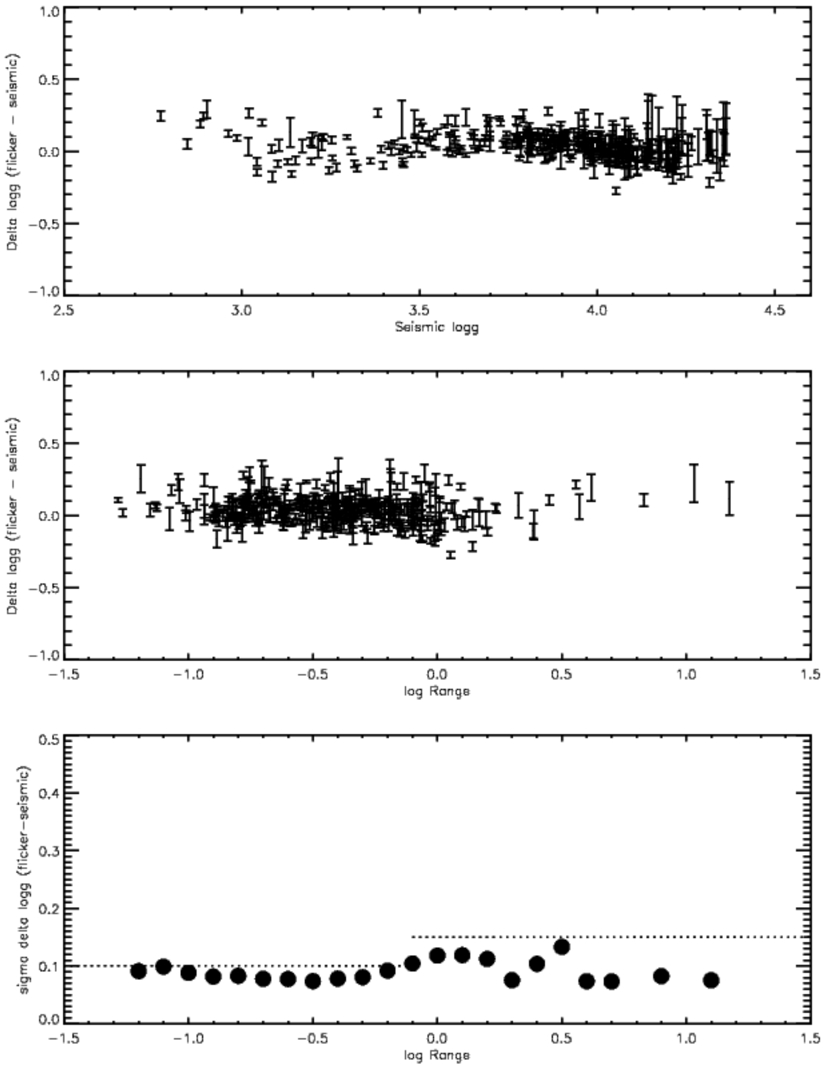

Figure 5.5: Comparisons between F_8 and asteroseismic g. We use the asteroseismic sample of Kepler stars [36] initially used to calibrate the F_8-based g [20]. In each panel, the error bars on the F_8-based g are determined from the scatter in the F_8-based g from multiple quarters of Kepler light curves. The bottom panel shows that the agreement between the F_8 and asteroseismic g values is a function of the overall photometric variability of the stars (R_{var}). Stars with $R_{var} < 1$ ppt show a constant scatter of ∼0.1 dex in log$g$, whereas stars with $R_{var} > 1$ ppt show a slightly elevated scatter of ∼0.15 dex.

REFERENCES

[1] Ábrahám, P., Kóspál, Á., Csizmadia, Sz., Moór, A., Kun, M., Stringfellow, G. 2004, A&A, 419, 39

[2] Acosta-Pulido, J. A., et al. 2007, AJ, 133, 2020

[3] Aigrain, S. & Irwin, M. 2004, MNRAS, 350, 331

[4] Aigrain, S., Pont, F., Zucker, S. 2012, MNRAS, 419, 3147

[5] Akeson, R. L. et al. 2013, PASP, 125, 989

[6] Akritas, M. G., Murphy, S. A. & LaValley, M. P. 1995, Journal of American Statistical Association, 90, 170

[7] Akritas, M. G. & Siebert, J. 1996, MNRAS, 178, 919

[8] Aspin, C., Barbieri, C., Boschi, F., Di Mille, F., Rampazzi, F., Reipurth, B., & Tsvetkov, M. 2006, AJ, 132, 1298

[9] Aspin, C., Beck, T., & Reipurth, B. 2008, AJ, 135, 423

[10] Aspin, C., Greene, T., & Reipurth, B. 2009, AJ, 137, 2968

[11] Auvergne, M. et al. 2009, A&A, 506, 411

[12] Baliunas, S. L. et al. 1995, ApJ, 438, 269

[13] Bakos, G. *Á* et al. 2010, ApJ, 710, 1724

[14] Ballard, S. et al. 2011, ApJ, 743, 200

[15] Barnes, S. 2003, ApJ, 586, 464

[16] Barnes, S. 2007, ApJ, 669, 1167

[17] Basri, G. et al. 2010, ApJ, 713, L155

[18] Basri, G. et al. 2011, AJ, 140, 20

[19] Basri, G., Walkowicz, L. M. & Reiners, A. 2013, ApJ, 769, 37

[20] Bastien, F. A., Stassun, K. G., Basri, G., Pepper, J. 2013, Nature, 500, 427

[21] Bastien, F. A. et al. 2014, AJ, 147, 29

[22] Batalha, N. M. et al. 2011, ApJ, 729, 27

[23] Batalha, N. M. et al. 2013, ApJ204, 24

[24] Boisse, I., Bonfils, X. & Santos, N. C. 2012, A&A, 545, 109

[25] Borucki, W. J. et al. 2010, Science, 327, 977

[26] Borucki, W. et al. 2011, ApJ, 736, 19

[27] Borucki, W. J. et al. 2013, Science, 340, 587

[28] Briceño, C., et al. 2004, ApJ, 606, L123

[29] Brown, T. M., Gilliland, R. L., Noyes, R. W. & Ramsey, L. W. 1991, ApJ, 368, 599

[30] Brown, T. M. & Gilliland, R. L. 1994, Ann. Rev. Astron. Astrophys, 32, 37

[31] Brown, T. M., Latham, D. W., Everett, M. E., Esquerdo, G. A. 2011, AJ, 142, 112

[32] Burger, D. et al. Astron. Comput, in press.

[33] Butler, R. P., Marcy, G. W., Williams, E., McCarthy, C., Dosanjh, P., Vogt, S. S. 1996, PASP, 108, 500

[34] Chaplin, W. J., Elsworth, Y., Isaak, G. R., Miller, B. A. & New, R. 2000, MNRAS, 313, 32

[35] Chaplin, W. J. et al. 2011, ApJ, 732, L5

[36] Chaplin, W. J. et al. 2011, Science, 332, 213

[37] Chaplin, W. J. & Miglio, A. 2013, Ann. Rev. Astron. Astrophys., 51, 353

[38] Christensen-Dalsgaard, J. 2004, Sol. Phys., 220, 137

[39] Cochran, W. D. et al. 2002, AJ, 124, 565

[40] Cox, A. N. 2000, Allen's Astrophysical Quantities (AIP Press)

[41] Cox, J. P. 1980, Theory of Stellar Pulsation, Princeton University Press, Princeton, New Jersey

[42] Cranmer, S. R., Bastien, F. A., Stassun, K. G., Saar, S. H. 2014, ApJ, 781, 124

[43] Curtis, J. L. et al. 2013, AJ, 145, 134

[44] D'Antona, F. & Mazzitelli, I. 1994, ApJS, 90, 467

[45] Dobrotka, A., et al. 2010, MNRAS, 402, 2567

[46] Dumusque, X., Udry, S., Lovis, C., Santos, N. C., Monteiro, M. J. P. F. G. 2011, A&A, 525, A140

[47] Dumusque, X., Santos, N. C., Udry, S., Lovis, C., Bonfils, X. 2011, A&A, 527, A82

[48] Duncan, D. K. et al. 1991, ApJS, 76, 383

[49] Endl, M. et al. 2011, ApJS, 197, 13

[50] Everett, M. E., Howell, S. B., Silva, D. R. & Szkody, P. 2013, ApJ, 771, 107

[51] Frohlich, C. et al. 1997, Sol. Phys. 170, 1

[52] Gaidos, E. & Mann, A. W. 2013, ApJ, 762, 41

[53] Garcia, R. A. et al. 2010, Science, 329, 1032

[54] Ghezzi, L. et al. 2010, ApJ720, 1290

[55] Gilliland, R. L. 2008, AJ, 136, 566

[56] Gilliland, R. L., et al. 2011, ApJS, 197, 6

[57] Gilliland, R. L. et al. 2013, ApJ, 766, 40

[58] Girardi, L., Groenewegen, M. A. T., Hatziminaoglou, E. & da Costa, L. 2005, A&A, 436, 895

[59] Greene, T. & Lada, C. 1997, AJ, 114, 2157

[60] Hartman, J. D. et al. 2011, ApJ, 742, 59

[61] Helsel, D. R. 2005, Nondetects and Data Analysis: Statistics for Censored Environmental Data (John Wiley and Sons)

[62] Henry, G. W., Fekel, F. C., Henry, S. M. & Hall, D. S. 2000, ApJS, 130, 201

[63] Herbst, W., Bailer-Jones, C. A. L., Mundt, R., Meisenheimer, K., & Wackermann, R. 2002, A&A, 396, 513

[64] Herbst, W., & Wittenmyer, R. 1996, BAAS, 189, no.4908

[65] Herbst, W., Herbst, D. K., Grossman, E. J., & Weinstein, D. 1994, AJ, 108, 1906

[66] Hirota, T., et al. 2007, PASJ, 59, 897

[67] Howard, A. W. et al. 2010, ApJ, 721, 1467

[68] Howard, A. W. et al. 2012, ApJS, 201, 15

[69] Howell, S. B. et al. 2012, ApJ, 746, 123

[70] Huber, D. et al. 2011, ApJ, 743, 143

[71] Huber, D. et al. 2013, ApJ, 767, 127

[72] Isaacson, H. & Fischer, D. 2010, ApJ, 725, 875

[73] Johnson, J. A. et al. 2007, ApJ, 665, 785

[74] Kalirai, J. S. et al. 2001, AJ, 122, 266

[75] Kalirai, J. S. et al. 2007, ApJ, 671, 748

[76] Kalirai, J. S. et al. 2008, ApJ, 676, 594

[77] Karoff, C., & Kjeldsen, H. 2008, ApJ, 678, L73

[78] Kenyon, S. & Hartmann, L. 1995, ApJS, 101, 117

[79] Kenyon, S., Kolotilov, E. A., Ibragimov, M. A., & Mattei, J. A. 2000, ApJ, 531, 1028

[80] Kienreich, I. W., Temmer, M., & Veronig, A. M. 2009, ApJ, 703, L118

[81] Kjeldsen, H. & Bedding, T. R. 1995, A&A, 293, 87

[82] Kjeldsen, H. & Bedding, T. R. 2011, A&A, 529, L8

[83] Komm, R. W., Howe, R. & Hill, F. 2000, ApJ, 531, 1094

[84] Kraus, S., et al. 2007, A&A, 466, 649

[85] Kurtz, D. W., 2006, in ASP Conf. Ser., Astrophysics of Variable Stars, eds., C. Sterken & C. Aerts, 347, 101

[86] Lockwood, G. W., Skiff, B. A., & Radick, R. R. 1997, ApJ, 485, 789

[87] Lomb, N. R. 1976, Ap&SS, 39, 447

[88] Mann, A. W., Gaidos, E., Lpine, S. & Hilton, E. J. 2012, ApJ, 753, 90

[89] Martínez-Arnáiz, R., Maldonado, J., Montes, D., Eiroa, C., & Montesinos, B. 2010, A&A, 520, A79

[90] Massarotti, A., Latham, D. W., Stefanik, R. P. & Fogel, J. 2008, AJ, 135, 209

[91] Mathur, S. et al. 2011, ApJ, 741, 119

[92] Mauche, C. 1997, in ASP Conf. Ser., Accretion Phenomena and Related Outflows, ed., D. T. Wickramasinghe, L. Ferrario, & G. V. Bicknell, 121, 251

[93] McNeil, J. 2004, IAU Circ. 8284

[94] McQuillan, A., Aigrain, S., & Roberts, S. 2012, A&A, 539, A137

[95] McQuillan, A., Aigrain, S. & Mazeh, T. 2013, MNRAS, 432, 1208

[96] McQuillan, A., Mazeh, T. & Aigrain, S. 2014, ApJSin press.

[97] Meibom, S. et al. 2013, Nature, 499, 55

[98] Menten, K. M., Reid, M. J., Forbrich, J., & Brunthaler, A. 2007, A&A, 474, 515

[99] Meunier, N., Desort, M. & Lagrange, A.-M. 2010, A&A, 512, 39

[100] Mitchell, D. S. et al. 2013, A&A, 555, 87

[101] Muzerolle, J., Megeath, S. T., Flaherty, K. M., Gordon, K. D., Rieke, G. H., Young, E. T., & Lada, C. J. 2005, ApJ, 620, L107

[102] Noyes, R. W., Hartmann, L. W., Baliunas, S. L., Duncan, D. K., & Vaughan, A. H. 1984, ApJ, 279, 763

[103] Queloz, D. et al. 2001, A&A, 379, 279

[104] Petigura, E. A., Marcy, G. W. & Howard, A. W. 2013, ApJ, 770, 69

[105] Pinsonneault, M. et al. 2012, ApJS, 199, 30

[106] Pont, F., Aigrain, S. & Zucker, S. 2011, MNRAS, 411, 1953

[107] Press, W. H. 1978, Comments on Astrophysics, 7, 103

[108] Press, W. H., Teukolsky, S. A., Vetterling, W. T., & Flannery, B. P. 1992, Numerical Recipes in Fortran, Second Edition (Cambridge: Cambridge Univ. Press), 621

[109] Pretorius, M., Warner, B., & Woudt, P. 2006, MNRAS, 368, 361

[110] Radick, R. R., Lockwood, G. W., & Baliunas, S. L. 1990, Science, 247, 39

[111] Radick, R. R., Lockwood, G. W., Skiff, B. A., & Baliunas, S. L. 1998, ApJS, 118, 239

[112] Reinhold, T., Reiners, A. & Basri, G. 2013, A&A, 560, 4

[113] Rucinski, S., et al. 2008, MNRAS, 391, 1913

[114] Rutten, R. G. M. 1984, A&A, 130, 353

[115] Saar, S. H. & Donahue, R. A. 1997, ApJ, 485, 319

[116] Saar, S. H., Butler, R. P., & Marcy, G. W. 1998, ApJ, 498, L153

[117] Saar, S. H. & Fischer, D. 2000, ApJ, 534, L105

[118] Saar, S. H. 2003, ASP Conference Series, 294

[119] Santos, N. C. et al. 2000, A&A, 361, 265

[120] Scargle, J. D. 1982, ApJ, 263, 835

[121] Schroder, C., Reiners, A. & Schmitt, J. H. M. M. 2009, A&A, 493, 1099

[122] Shu, F. H., Najita, J., Ruden, S. P., & Lizano, S. 1994, ApJ, 429, 781

[123] Skumanich, A. 1972, ApJ, 171, 565

[124] Stassun, K. G., van den Berg, M., Mathieu, R. D., & Verbunt, F. 2002, A&A, 382, 899

[125] Stassun, K. G., Mathieu, R. D., Mazeh, T., & Vrba, F. J. 1999, AJ, 117, 2941

[126] Stello, D. et al. 2013, ApJ, 765, L41

[127] Strassmeier, K. G. & Hall, D. S. 1988, ApJS, 67, 439

[128] Strassmeier, K. G. & Hall, D. S. 1988, ApJS, 67, 453

[129] Strassmeier, K. G. 2009, Astron. Astrophys. Rev., 17, 251

[130] Tassoul, M., & Tassoul, J. L., 1968, ApJ, 153, 127

[131] Toma, E. 1972, A&A, 19, 76

[132] Torres, G., Andersen, J. & Gimnez, A. 2010, Astron. Astrophys. Rev., 18, 67

[133] Turnbull, B. W. 1976, Journal of the Royal Statistical Society. Series B, 38, 290

[134] Valenti, J. A. & Fischer, D. A. 2005, ApJS, 159, 141

[135] Verner, G. A. et al. 2011, ApJ, 738, 28

[136] Vogt, S. S. et al. 1994, Proc. SPIE, 2198, 362

[137] Walker, G. et al. 2003, PASP, 115, 1023

[138] Walkowicz, L. & Basri, G. 2013, MNRAS, 436, 1883

[139] Warner, B., Pretorius, M. 2008, MNRAS, 383, 1469

[140] Warner, B., Woudt, P. 2002, MNRAS, 335, 84

[141] Woudt, P. A., & Warner, B. 2002, MNRAS, 333, 411

[142] Wright, J. T., Marcy, G. W., Butler, R. P., Vogt, S. S. 2004, ApJS, 152, 261

[143] Wright, J. T. 2005, PASP, 117, 657